

Submitted to ApJ 17 June 2004.
 Manuscript pages : 40, Figures: 13

Phase light curves for extrasolar Jupiters and Saturns

Ulyana A. Dyudina^{1,2}, Penny D. Sackett², Daniel D. R. Bayliss³

*Research School of Astronomy and Astrophysics, Mount Stromlo Observatory, Australian
 National University, Cotter Road, Weston, ACT, 2611, Australia*

Sara Seager

DTM, Carnegie Institute at Washington, DC , USA

Carolyn C. Porco

CICLOPS/Space Science Institute, Boulder, CO, USA

Henry B. Throop and Luke Dones

Southwest Research Institute, Boulder, CO, USA

ABSTRACT

We predict how a remote observer would see the brightness variations of giant planets similar to those in our Solar System as they orbit their central stars. We model the geometry of Jupiter, Saturn and Saturn's rings for varying orbital and viewing parameters. Scattering properties for the planets and rings at wavelengths 0.6-0.7 microns are assumed to follow those observed by Pioneer and Voyager spacecraft, namely, planets are forward scattering and rings are backward scattering. Images of the planet with or without rings are simulated and used to calculate the disk-averaged luminosity varying along the orbit, that is, a light curve is generated. We find that the different scattering properties of Jupiter and Saturn (without rings) make a substantial difference in the shape of their light curves. Saturn-size rings increase the apparent luminosity of the planet by a factor of 2-3 for a wide range of geometries, an effect that could be confused with a larger planet size. Rings produce asymmetric light curves

¹NASA/Goddard Institute for Space Studies, 2880 Broadway, New York, NY, 10025, USA

²Planetary Science Institute, Australian National University, ACT, 0200, Australia

³Victoria University of Wellington, New Zealand

that are distinct from the light curve of the planet without rings, which could resolve this confusion. If radial velocity data are available for the planet, the effect of the ring on the light curve can be distinguished from effects due to orbital eccentricity. Non-ringed planets on eccentric orbits produce light curves with maxima shifted relative to the position of the maximum planet’s phase. Given radial velocity data, the amount of the shift restricts the planet’s unknown orbital inclination and therefore its mass. Combination of radial velocity data and a light curve for a non-ringed planet on an eccentric orbit can also be used to constrain the surface scattering properties of the planet and thus describe the clouds covering the planet. To summarize our results for the detectability of exoplanets in reflected light, we present a chart of light curve amplitudes of non-ringed planets for different eccentricities, inclinations, and the viewing azimuthal angles of the observer.

Subject headings: scattering; methods: data analysis; planets: rings; planets: Jupiter, Saturn;(stars:) planetary systems; cosmology: observations

1. Introduction

Modern space-based telescopes and instrumentation are now approaching the precision at which reflected light from extrasolar planets can be detected directly (Jenkins & Doyle 2003; Walker et al. 2003; Green et al. 2003; Hatzes 2003). Since 1995, meanwhile, more than 100 extrasolar planets (or exoplanets) have been detected indirectly by measuring the reflex motion of their parent star along the line of site (radial velocity or Doppler method). One of these radial velocity planets, Gl876b, has been confirmed by measuring the parent star motion on the sky (astrometry) (Benedict et al. 2002), and a second, HD209458b, by measuring the change in parent star brightness as the planet executes a transit of its host (transit photometry) (Charbonneau et al. 2000; Henry et al. 2000; Udalski et al. 2002a,b, 2003). Three exoplanets have now been detected by transit photometry (Konacki et al. 2003, 2004; Bouchy et al. 2004), and then confirmed with Doppler measurements. It is expected that in the next decade, as photometric techniques are improved both from the ground and in space, direct detection of the reflected light from exoplanets will not only prove useful in expanding the number of exoplanets known, but also in detailing their characteristics.¹

Reflected light from an exoplanet can be detected in two ways. First, with sufficient spatial resolution, direct imaging can resolve the planet and the star in space, and the projection of its orbit traced as a function of time simultaneously with the measurement of

¹Reviews and references on extrasolar planets and detection techniques can be found at <http://www.obspm.fr/encycl/encycl.html>

the planet’s phases in reflected light. To be detected, the planets must be at large enough orbital distances to be easily resolved from their parent star, and yet close enough that the reflected brightness, which decreases as inverse square of the orbital distance, is large enough to be observed against the background in a reasonable amount of time. Even with coronagraphic or nulling techniques to help block the light at the position of the star itself, success will require optical point spread functions with very low level scattering wings to obtain sufficient reduction of parent starlight at the position of the planet. Consequently, the first extrasolar planets to be detected directly in this way are likely to be giants orbiting relatively nearby stars (tens of pc) at intermediate semi-major axes (1-5 AU) (Dekany et al. 2004; Lardi re et al. 2003; Codona & Angel 2004; Trauger et al. 2003; Krist et al. 2003; Clampin et al. 2001), where the contrast between planet and scattered starlight is high enough and yet the total reflected light still measurable. Since direct imaging can yield both the orbit and the luminosity of the planet simultaneously, it will be a robust detection method that will add greatly to our knowledge of planetary structure and evolution; Unfortunately direct exoplanet imaging from either the ground or space will not likely be available for a decade. In this paper, therefore, the applicability of our results to direct imaging is not described in detail, although our light curves can be used for planning future observations aimed at directly detecting spatially-resolved planets in reflected light.

The second method of detecting reflected light is precise, integrated photometry. This technique searches for temporal variations in the combined parent star and exoplanet (reflected) light curve as the planet changes phases during the orbit in the same way the Moon changes phase, producing a “phase light curve.” The vast majority of the light comes from the star itself, but if the periodic variations can be extracted from the total light curve, the planetary phase as a function of time can be deduced. Since the light from the parent star need not be blocked, if the signal to noise is large enough, planets much closer to their parent star can be detected then with spatially resolved imaging. Furthermore, in principle, more distant planetary systems and planets at smaller physical orbital radii can be studied in this way since the angular size of the point spread function does not present a limitation.

Ground-based based observations of known short-period exoplanets have used Doppler tomographic signal-analysis techniques to search for reflected light signatures in high-resolution spectroscopy. A combined, high signal-to-noise spectrum of the star is shifted and subtracted from individual spectra taken at different times (i.e., different phases of the exoplanet’s illumination). Since the planet contributes a different amount of reflected light to the combined spectrum as a function of orbital phase, one expects a residual in the subtracted spectra at a (exoplanet) velocity position that varies in sinusoidally with phase. In every case attempted to date, no signature of reflected light has been detected (Charbonneau et al. 1999; Collier Cameron et al. 2002; Leigh et al. 2003a; Leigh et al. 2003b). However, because the orbital phase is known from radial velocity measurements, the lack of detection constrains the grey geometric albedo p of the planet for an assumed phase curve, orbital inclination, and planetary radius. For the assumed parameters of τ Bootis b, HD 75289b, and the innermost

planet of ν And, observations non-detections seem to imply that $p < 0.4$ (Collier Cameron et al. 2002; Leigh et al. 2003a; Leigh et al. 2003b).

Current ground-based observations for reflected starlight from exoplanets are able to reach a precision of $\sim 10^{-5}$ (Leigh et al. 2003a,c), if the planetary reflection spectrum is fairly well known. Current and near-future space-based telescopes are capable of detecting variations of the order $10^{-4} - 10^{-6}$ of the total star light (Jenkins & Doyle 2003; Green et al. 2003), at the limit of what might be expected from the class of "hot Jupiter" planets, i.e., gas giants orbiting within 0.1 AU of their solar-type parent stars (Seager et al. 2000). With the advent of 30m-100m telescopes in the next 10-15 years, one might expect these limits to improve by factors of 10 to 100.

The shape of the phase light curve depends on many parameters: the planet's orbit, its geometry relative to the observer, the planet's oblateness, the scattering properties of the planet's surface, and the presence and geometry of rings. The amplitude of the light curve scales in a simple manner with planet's size and its orbital distance. When planning observations, it is important to understand the variety of shapes and amplitudes of these phase light curves and the conditions under which they will be generated: this is the purpose of this paper. In particular, the effects of planet size, oblateness, rings, and "surface" scattering properties, which convey information about atmospheric structure and reflecting clouds, will be superimposed in observed light curves and may be indistinguishable from one other, causing confusion or degeneracies in interpretation. We discuss these degeneracies and possible ways to eliminate them through detailed light curve measurements or alternative observations.

The great interest in the potential of exoplanet detection through either reflected light, reflected phase light curves, or transits is demonstrated by a number of works published in the last few years. Seager et al. (2000) modeled the atmospheric and cloud composition and simulated the light curves for close-in giant planets with various cloud coverage. Sudarsky et al. (2003) modeled clouds and spectra for extrasolar planets at different distances from the star. Barnes & Fortney (2003) modeled transit light curves for a planet with rings. Arnold & Schneider (2004) simulated light curves for planets with rings of different sizes, assuming planets with isotropically-scattering (Lambertian) surfaces and rings with isotropically scattering particles, and provide a discussion of the possibility of ring presence at different stages of planetary system evolution.

Our model is the first to use the *observed anisotropic scattering* of Jupiter, Saturn, and Saturn's rings. We find that anisotropic scattering yields light curves that are substantially different from those assuming Lambertian planets and rings, and thus is more likely to give an accurate description for extrasolar planets similar to Jupiter and Saturn. We do not model the spectral light curve dependence; our model produces light curves for averaged red visible light ($\sim 0.6-0.7\mu\text{m}$).

In Section 2 we describe our model. In Section 3 we present our light curves for non-

ringed exo-Saturn and exo-Jupiter planets on an edge-on circular orbit, for variously oriented oblate exo-Saturns, for a ringed planet (with Saturn-like scattering properties) at variously inclined circular orbits, and for both a non-ringed exo-Saturn and an exo-Jupiter on eccentric orbits. In Section 4, we discuss the uncertainties of our model and the detectability of the light curves by modern and future instruments. Conclusions are presented in Section 5.

2. Model

We model the observed red brightness of an exo-Jupiter or exo-Saturn by tracing how light rays from the central star are reflected by each position on the planet. We then produce images (maps with resolution of 16 to 200 pixels across, depending on the acceptable error level) of the planet and its rings at different geometries. The light rays from the star illuminating the planet are assumed to be parallel, consistent with both star and planet being negligible in size compared to the star-planet distance. The reflected rays collected by observer are assumed to be parallel, consistent with a remote observer. The model includes reflection from the planet and rings, and the rings’ transmission and shadows, but does not incorporate second order effects such as ring shine on the planet or planet shine on the rings. We account for planet’s oblateness in some of our simulations using the 10% oblateness of Saturn as an example.

The red scattering properties in our model are the average properties integrated along the planet’s spectrum, weighted by the wavelength-dependent transmissivity of the Pioneer red filter, which is non-zero in the range $0.595\text{--}0.720\mu\text{m}$. Our notation matches that of most observational papers on Saturn and Jupiter. For comparison of our results with those from models of Arnold & Schneider (2004), we list both our and their parameter names in Table 1.

Figure 1 demonstrates the geometry for a ringed planet on a circular orbit defined by the angles listed in Table 1. The only time-dependent parameters are the orbital angle Θ and phase angle α . For a non-ringed planet the star-planet-observer geometry is fully determined by two angles i and Θ (α is linked to i and Θ). For a ringed planet the geometry is determined by four angles: i , Θ , ω_r and ϵ .

2.1. Reflecting properties of Jupiter, Saturn and rings

Figure 2 shows the scattered brightness, for a given geometry, derived from our model for the surfaces of Jupiter, Saturn, and its the rings in red wavelengths ($0.6\text{--}0.7\mu\text{m}$). Note the logarithmic scale of the ordinate and the large amplitudes of the phase functions. The normalized brightness $I(\alpha, \mu_0, \mu)/(F \cdot \mu_0)$ of a point on the surface is plotted versus scattering phase angle α . $F \cdot \mu_0$ is the “ideal” reflected brightness of a white isotropically scattering

This work	Arnold & Schneider 2004	Quantity	Units (if any)
A, B		Coefficients of the Backstorm law	
a, a_1		Semi-major axis of the planet’s orbit	AU
D_P		Planet-star distance	km
E		Eccentric anomaly (polar angle parameterization)	
e		Eccentricity	
F	γ	Intensity of a white Lambertian surface ^a	$Wm^{-2}sr^{-1}$
g_1, g_2, f		Parameters of Henyey-Greenstein function	
I	L_p, I_R, I_T L_{ps}, L_{pr}	Intensity (or brightness, or radiance) of the surface	$Wm^{-2}sr^{-1}$
i	i	Inclination of the orbit (0°: face-on, 90°: edge-on)	degrees
L_P		Luminosity of the planet ^b	Wsr^{-1}
L_*		Luminosity of the star ^b	Wsr^{-1}
M		Mean anomaly (time parameterization)	
p		Full-disk albedo ^b $L_P/(\pi R_P^2 F)$	
R		Star’s magnitude in R band	
R_P	r_p	Equatorial radius of the planet	km
r_{pix}		Pixel size	km
V		Star’s magnitude in V band	
α	α	Phase angle	degrees
ϵ		Planet’s obliquity	degrees
Θ	$\phi = \Theta - 90^\circ$	Orbital angle ($\pm 180^\circ$: min phase, 0° : max phase)	degrees
μ_0, μ	μ_0, μ	Cosines of the incidence and emission angle	
ω		Argument of pericentre (90°: observed from pericentre, -90°: from apocentre)	degrees
ω_r		Observer’s azimuth relative to the rings	degrees

Table 1: Parameters used in modeling.

^a $F \cdot (\pi \text{ steradians})$ is the incident stellar flux at the planet’s orbital distance (which is also sometimes called F , but has Wm^{-2} units unlike our intensity F measured per unit solid angle).

^bThe ‘red’ or ‘blue’ optical properties are the convolution of the planet’s (or ring’s or solar) spectrum with the wavelength-dependent transmissivity of the Pioneer filter (which is nonzero between 0.595-0.720 μm for red filter and 0.390-0.500 μm for blue filter)

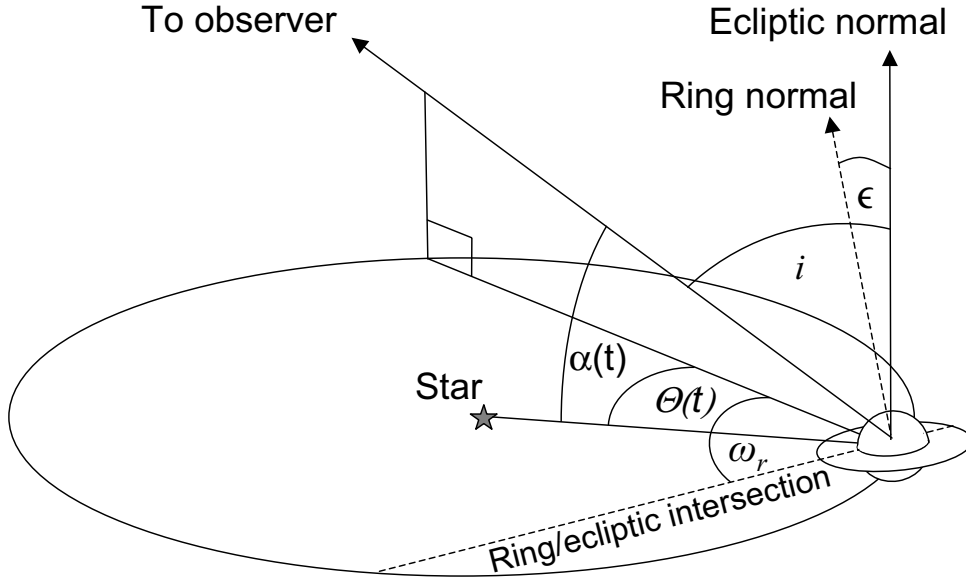


Fig. 1.— Angles defining the geometry of a ringed planet on a circular orbit observed from a large distance. Dashed lines are the normal to the ring plane and the line of intersection of the ecliptic with the ring plane. The observer's azimuth relative to the rings, ω_r , is positive when the rings are tilted from ecliptic towards the observer and negative when the rings are tilted from the ecliptic away from the observer and changes from -90° to 90° . We do not consider other possible values of $\omega_r = \pm(90 - 180)^\circ$ because these orientations produce light curves symmetric to those with $\omega_r = \pm(0 - 90)^\circ$. The geometry is fully determined by i and $\Theta(t)$ for a non-ringed planet and by i , $\Theta(t)$, ω_r , and ϵ for a ringed planet.

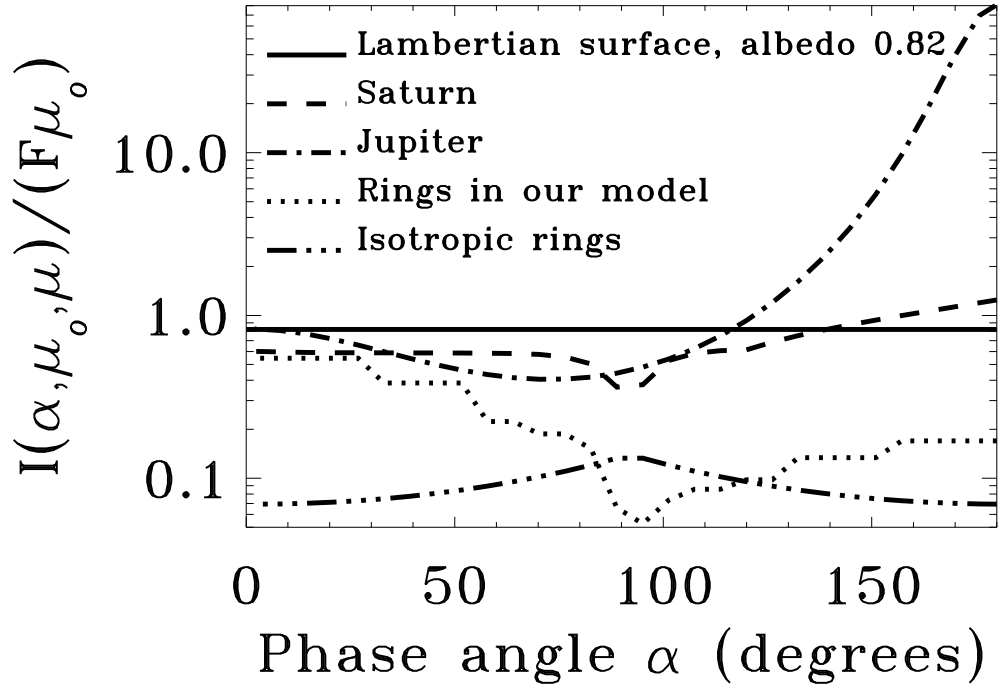


Fig. 2.— Scattering phase functions for a Lambertian surface, Saturn, Jupiter, Saturn’s rings (as used in our model), and the phase function for rings consisting of isotropically scattering particles used by Arnold & Schneider (2004). The phase functions are plotted for a single sample geometry: μ_0 is fixed (the Sun is 2° above horizon), while the observer moves in the plane that includes the Sun and zenith. The wavelengths correspond to visible red light ($0.6\text{--}0.7\mu\text{m}$).

(Lambertian) surface, where μ_0 is the cosine of the incidence angle measured from the local vertical. $F \cdot (\pi \text{ steradians})$ is a solar flux at the planet’s orbital distance. In our notation, $\alpha = 0^\circ$ indicates backward scattering and $\alpha = 180^\circ$ indicates forward scattering. Lambertian scattering with reflectivity 0.82 (matching Saturn’s full-disk albedo at opposition) is shown as a horizontal solid line for comparison. We also indicate, for the same ring opacity, albedo and geometry, the ring phase function used by Arnold & Schneider (2004), which assumes isotropically-scattering particles.

For Jupiter, we assume that the scattering phase function depends only on α . For Saturn with rings, the scattering phase function depends on three angles: incidence (via μ_0), emission (via μ), and phase (via α), and so cannot be described fully by the one-parameter function of α . Figure 2 shows reflected light only for the geometry in which the Sun is 2° above the horizon ($\mu_0=0.035$) and the observer moves from the Sun’s location ($\alpha = 0^\circ$) across the zenith toward the point on the horizon opposite to the Sun ($\alpha = 178^\circ$). The small amplitude for isotropically scattering rings in Fig. 2 is due to the very grazing illumination chosen for this example. At less grazing illuminations, the amplitudes for isotropic rings and our rings are more similar.

2.1.1. *Jupiter*

For each point on Jupiter, the strong forward scattering of the reflecting clouds is represented by the two-term Henyey-Greenstein function $P(g_1, g_2, f, \alpha)$.

$$I(\alpha, \mu_0, \mu)/F = \mu_0 \cdot P(g_1, g_2, f, \alpha) \quad (1)$$

$$P(g_1, g_2, f, \alpha) = f P_{HG}(g_1, \alpha) + (1 - f) P_{HG}(g_2, \alpha) \quad (2)$$

The individual terms are Henyey-Greenstein functions representing forward and backward scattering lobes, respectively.

$$P_{HG}(g, \alpha) = 2 \cdot \frac{(1 - g^2)}{(1 + g^2 + 2g \cdot \cos \alpha)^{3/2}} \quad , \quad (3)$$

where α is the phase angle, f is the fraction of the forward versus backward scattering, and g is one of g_1 or g_2 ; g_1 is positive and controls the sharpness of the forward scattering lobe and g_2 is negative and controls the sharpness of the backscattering lobe. Note that we have rewritten P_{HG} relative to common notation in which the scattering angle $\theta = 180^\circ - \alpha$ is used; this reverses the sign in front of the $2g \cdot \cos \alpha$ term. Unlike the common use of the Henyey-Greenstein function for single-particle scattering, in which the function is normalized over the sphere of solid angles around the particle, we use this function only as a convenient analytical expression to fit the measured scattering of Jupiter’s surface. In this case, the function is not normalized over the hemisphere of solid angles above the surface. The spherical albedo (the ratio of reflected to incident light for the whole planet at appropriate wavelengths) is

imbedded in the scattering function, and is a rather complicated integral over the planet’s surface that we do not calculate here.

Figure 3 shows our fit of the Henyey-Greenstain function, with $g_1 = 0.8$, $g_2 = -0.38$, and $f = 0.9$, to the data points from the Pioneers 10 and 11 images (Tomasko et al. 1978; Smith & Tomasko 1984). The values we have chosen for g_1 , g_2 , and f also reproduce the full-disk albedos in the spectra observed by Karkoschka (1994) and Karkoschka (1998) at the wavelengths corresponding to the red passband of Pioneer. Pioneer images are taken with broadband blue (0.390–0.500 μm) and red (0.595–0.720 μm) filters at different locations on Jupiter. In particular, Tomasko et al. (1978) and Smith & Tomasko (1984) have indicated two types of locations: the belts, usually seen as dark stripes on Jupiter (\times symbols on the plot), and zones, usually seen as bright stripes on Jupiter (+ symbols on the plot). The relative calibration between Pioneer 10 and Pioneer 11 data is not as well constrained as the calibration within each data set.

Accepting the calibrations given in Tomasko et al. (1978) for Pioneer 10 and Smith & Tomasko (1984) for Pioneer 11, our model curve better represents the observations in the red filter (black data points) than in the blue. We assume here that this curve represents the red wavelengths. The Pioneer 11 blue data at moderate α in Fig. 3 seem to be systematically offset from the Pioneer 10 points, which may be a result of relative calibration error. Consequently, we do not model the blue wavelengths.

The vertical spread of the points in the same filter and at the same location is due mainly to differences in emission and incidence angle between the points. This spread is not large, i.e., the reflectivity is not strongly dependent on incidence and emission angles for fixed α other than a $1/\mu_0$ dependence, which is often labeled “Lambertian limb-darkening.” We note, however, that the Pioneer-measured phase angle dependence is strongly non-Lambertian, which has important consequences for the light curves we generate.

In addition to Pioneer data, images of Jupiter from a variety of angles were taken by Voyager, Galileo, and Cassini, though we are not aware of any other published data of the scattering phase functions for the Jovian surface.² Data for $\alpha > 150^\circ$ do not exist because these directions would risk pointing spacecraft cameras too close to the Sun; this limits the ability of the data to constrain the forward-scattering peak at $\alpha \sim 180^\circ$. Our derived light curves are not severely affected by this uncertainty, however, since when the forward scattering is important, the observed crescent is small, and reflected light phase curve undergoes its minimum.

²One of us, UD, plans to work on obtaining the spectral phase functions from Cassini nine-filter visible images in the immediate future.

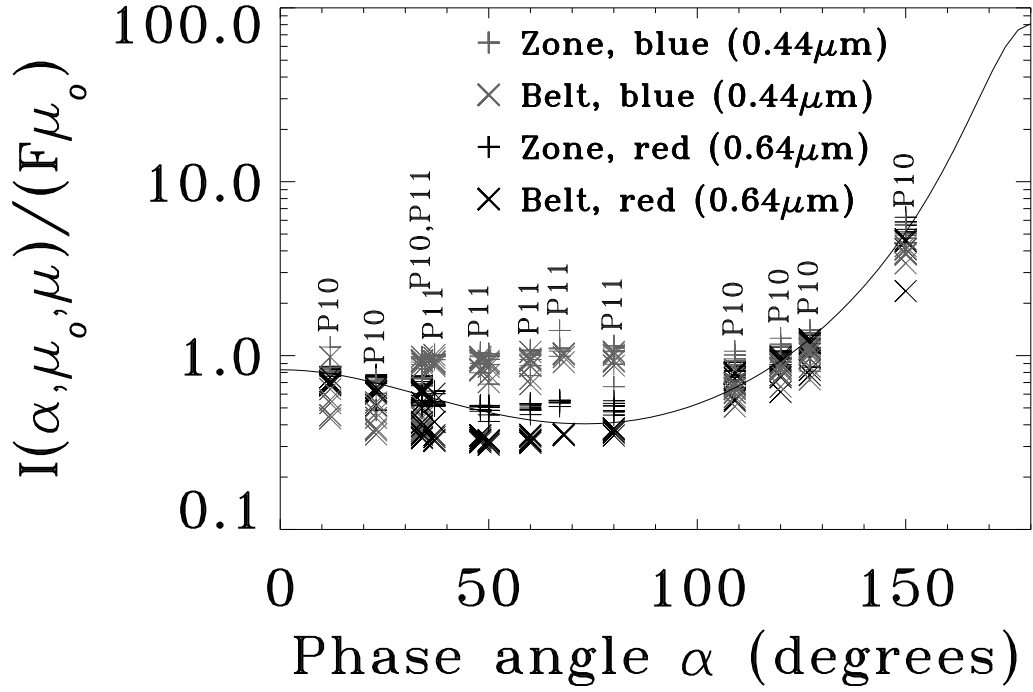


Fig. 3.— Our fit of the Henyey-Greenstein function (solid line, $g_1 = 0.8$, $g_2 = -0.38$, $f = 0.9$) to the Pioneer 10 data (labeled P10) published as Tables IIa and IIb of Tomasko et al. (1978), and Pioneer 11 data (labeled P11) published as Tables IIa and IIb of Smith & Tomasko (1984). The data represent belts (dark stripes) and zones (bright stripes) on Jupiter observed with the red ($0.595\text{--}0.720\ \mu\text{m}$) and blue ($0.390\text{--}0.500\ \mu\text{m}$) filters.

2.1.2. Saturn

The scattering phase function and albedo of Saturn are represented by the Backstorm law, which was used by Dones et al. (1993) to fit Saturn’s data.

$$I/F = \frac{A}{\mu} \left(\frac{\mu \cdot \mu_0}{\mu + \mu_0} \right)^B, \quad (4)$$

where μ and μ_0 are the cosines of emission and incident angles measured relative to the local vertical, respectively, and A and B are coefficients that depend on the phase angle α . The coefficients are fitted by Dones et al. (1993) to Pioneer 11 fitted phase function tables, which were produced by the multiple scattering model of Tomasko & Doose (1984). We averaged the coefficients published by Dones et al. (1993) separately for zones and belts through Pioneer’s blue and red filters.

Table 2 gives the resulting coefficients; Fig. 2 displays the red filter curve only.

Phase angle α	0°	30°	60°	90°	120°	150°	180° ^a
A (red, 0.64 μm)	1.69	1.59	1.45	1.34	1.37	2.23	3.09 ^a
B (red, 0.64 μm)	1.48	1.48	1.46	1.42	1.36	1.34	1.31 ^a
A (blue, 0.44 μm)	0.63	0.59	0.56	0.56	1.69	1.86	3.03 ^a
B (blue, 0.44 μm)	1.11	1.11	1.15	1.18	1.20	1.41	1.63 ^a

Table 2: Coefficients for the Backstorm function for Saturn, averaged between belt and zone values published in Table V of Dones et al. (1993).

^aThe coefficients at $\alpha=180^\circ$ are not constrained by observations; and were estimated by linearly extrapolating the coefficients at 120° and 150°

The Pioneer spacecraft did not observe Saturn at $\alpha > 150^\circ$. Corresponding coefficients in Dones et al. (1993) are given for α up to 150° . To complete the phase curve, we extrapolate the coefficients at 180° linearly from their values at 120° and 150° . The phase curve given in Fig. 2 corresponds to the case when the incidence angle is fixed at 88° (the Sun is 2° above the horizon, i.e., $\mu_0=0.035$) and the trajectory of the observer on the sky is in the plane including zenith and Sun’s location (μ is linearly dependent on α). This cross-section of the fitted three-parameter phase function is not as smooth as the Henyey-Greenstein function for Jupiter. For example, the dip at $\alpha = 90^\circ$ is a result of the approximation by an analytic function rather than real observations.

Figure 4 demonstrates the difference between the blue and red phase functions for Saturn. The values for the blue curve are 1.5 – 2 times smaller, indicating that Saturn is darker in blue wavelengths due to higher absorption by photochemical hazes.

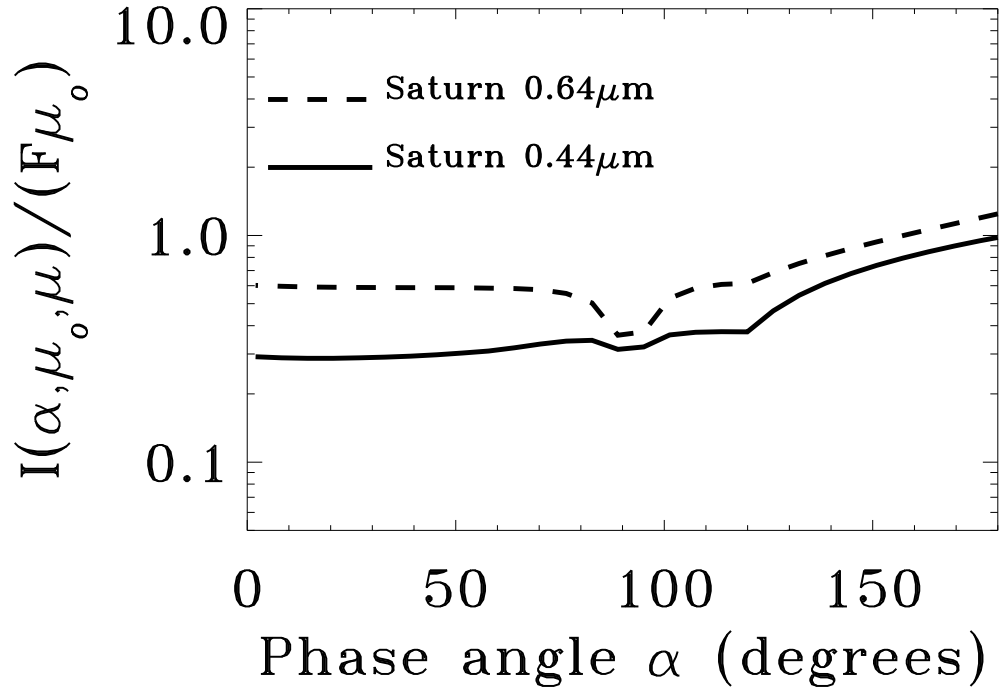


Fig. 4.— Scattering phase functions for Saturn in red ($0.595 - 0.720 \mu\text{m}$) and blue ($0.390 - 0.500 \mu\text{m}$) passbands adopted from Dones et al. (1993).

The ring brightness in reflection (top-side) and transmission (bottom-side) is provided by a physical scattering model of the ring. This model calculates multiple scattering within the rings using a ray tracing code. The model ring is populated with macroscopic bodies of 1m-size, with optical depth and albedo profiles chosen to match those of Dones et al. (1993). Note that Dones et al. (1993) found the amount of dust in the main rings to be too small to contribute substantially to ring reflection. The model reproduces well the brightnesses observed by Voyager 1 and 2. We use the code to predict ring brightness at geometries not observed by Voyager. The opacity for each pixel is taken at the point on the rings that projects to the pixel’s center.

The ring brightness at each point is a function of three angles (α, μ, μ_0), the optical depth, and the albedo. Due to data volume restrictions we have binned output in rather large steps, which depend on parameter values. These steps are clearly seen in the ring phase function (dotted line) in Fig. 2. The phase function in Fig. 2 corresponds to the same scattering geometry as the curves for Saturn shown in Fig. 4. The optical depth at the sample point on the rings (1.7 times Saturn’s radii from the planet’s center) is 2.3, the albedo of the ring particles is 0.56. The ring is observed from the illuminated side.

To produce light curves of the fiducial exoplanets that we model, images of the planet for a set of locations along the orbit are generated.

For each image we integrate the total light coming from the planet and the rings (if any) to obtain the full-disk (or geometric) albedo $p(\alpha)$.

$$p(\alpha) = \frac{\sum_{\text{pixels}} I(\mu, \mu_0, \alpha) \cdot r_{\text{pix}}^2 / F}{\pi R_P^2} \quad , \quad (5)$$

where r_{pix} is the pixel size and R_P is the planet’s radius. The full-disk albedo is the planet’s luminosity L_P normalized by the reflected luminosity of a Lambertian disk with the planet’s radius at the planet’s orbital distance, illuminated and observed from the normal direction.

$$p \equiv L_P / (\pi R_P^2 F) \quad (6)$$

Generally, I , L_P , F , and p depend on wavelength. However since we have integrated over the red passband, these values are weighted averages over the Pioneer filter at red wavelengths.

2.2. Eccentric Orbits

In addition to modeling light curves from ringed planets traveling in circular orbits, we also model the light curves of non-ringed planets moving in eccentric orbits. Although most of the planets in the Solar system orbit the Sun with low eccentricities, the extrasolar planets detected to date display a wide range of eccentricities³.

³Eccentricities of extrasolar planets are listed at <http://exoplanets.org/almanacframe.html>

Eccentric orbits differ from circular orbits in two main respects. First, the distance between the star and the planet varies according to the planet’s orbital position. As the planet moves from its pericentre to its apocentre, its separation from its host star increases. Second, in an eccentric orbit, the planet does not move with a constant angular speed around the star as it would in a circular orbit. The planet’s angular speed varies throughout the orbit, being a maximum at the pericentre and minimum at the apocentre.

To model the reflected light as a function of time, we calculate the angular position of the planet and the planet-star separation over a complete period using a solution to Kepler’s equation (in notation of Murray & Dermott (2001)):

$$M = E - e \sin E \quad (7)$$

where M is the mean anomaly (a parameterization of time), E is the eccentric anomaly (a parameterization of the polar angle) and e is the eccentricity. Kepler’s equation is transcendental in E and therefore cannot be solved directly. Since we need only one complete orbit to model a light curve, however, we are able to use the simple Newton-Ralpson method to obtain a numerical solution to Kepler’s equation. Applying the Newton-Ralpson method⁴ to Eq. 7 we obtain the iterative solution:

$$E_{i+1} = E_i - \frac{E_i - e \sin E_i - M_i}{1 - e \cos E_i} \quad (8)$$

Using this iteration, we calculate the angular position and planet-star separation as functions of time, and use this to model the amplitude of reflected light from the planet.

As can be seen in Fig. 5, the geometry of an ellipse introduces an additional parameter, in addition to inclination, in the observer’s azimuthal perspective of the system. This parameter is the argument of pericentre ω , which is the angle (in the planet’s orbital plane) between the ascending node line and pericentre (Murray & Dermott 2001). The reference plane is formed by the observer’s line of site and its normal in the ecliptic plane, which is also the accending node line. Viewing the system from the line of the pericentre (planet’s smallest phase is at pericentre) would give argument of pericentre 90° . Viewing the system from the line of the apocentre (planet’s largest phase is at pericentre) would give argument of pericentre -90° .

3. Results

We modeled several geometries for the planetary system, i.e., different orbital eccentricities e for non-ringed planets, and different ring obliquities ϵ relative to the ecliptic for

⁴Application of Newton-Ralpson method to Kepler’s equation is described in Murray & Dermott (2001)

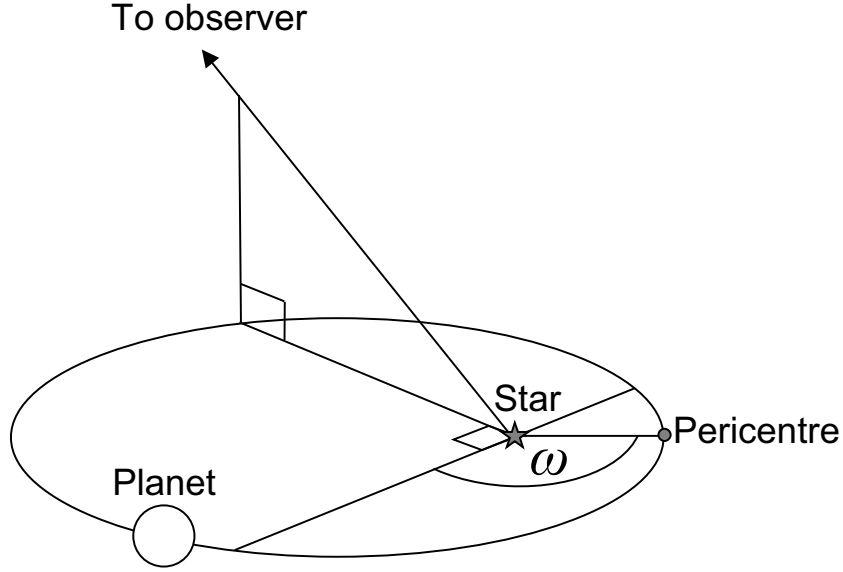


Fig. 5.— The argument of pericentre, ω , is an additional angle needed to define geometry of a non-ringed planet on eccentric orbit.

ringed planets on circular orbits. For each of these cases we modeled a variety of observer locations, i.e., different orbital inclinations i as seen by the observer, and different azimuths ω of the observer relative to the orbit’s pericentre or to the rings (ω_r). In what follows, we compare light curves for these differing geometries, and discuss whether or not different geometric effects can be distinguished from one another from the characteristics of the light curve alone.

3.1. Jupiter versus a ringless Saturn

We first tested how light curves would differ for (ringless) exoplanets with the surface reflection characteristics of Jupiter and Saturn. We modeled the planets for a variety of inclinations, assuming circular orbits. Low-inclination orbits (close to face-on) produce smaller light curve amplitudes because the planet appears to be at half-phase most of the time. The most prominent amplitudes, and the most prominent difference between Jupiter and Saturn reflectance properties, occurs for edge-on orbits, for which the phase changes from completely “new moon” to completely “full moon”.

Figure 6 compares edge-on light curves for a ringless Saturn, Jupiter, and a Lambertian planet. The luminosity of the planet is normalized by the incident stellar illumination to obtain the full-disk albedo p as described in equations (5) and (6). The planets are spherical and have identical radii; the curves differ only because of the different surface scattering of

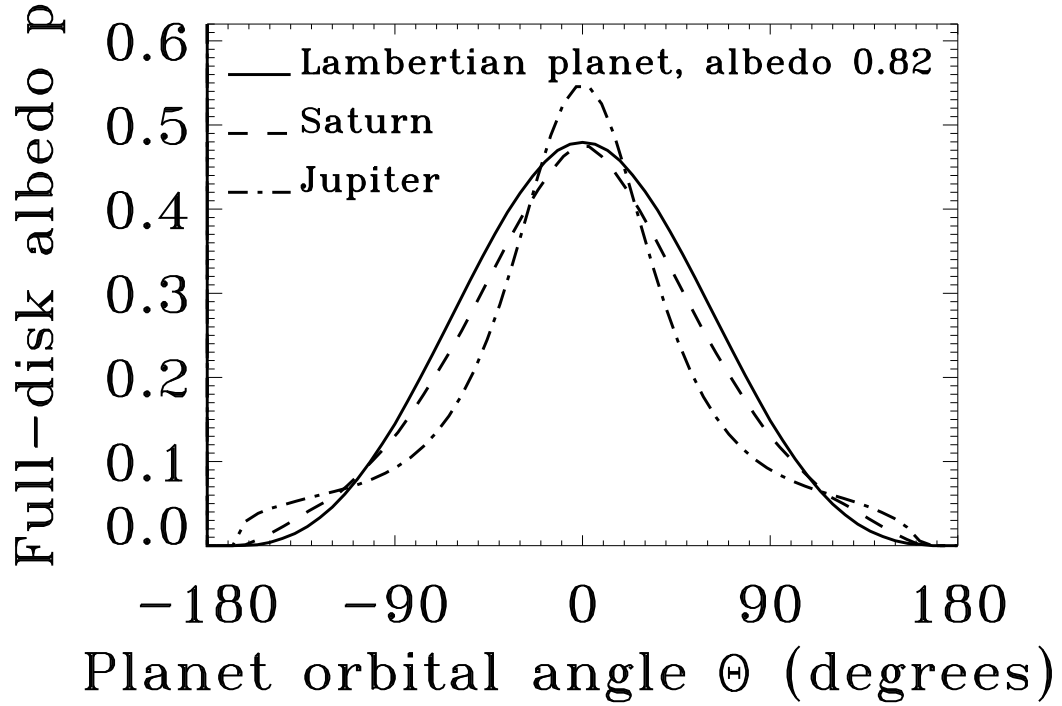


Fig. 6.— Comparison of light curves for a spherical Jupiter, a spherical Saturn , and a spherical Lambertian (isotropically scattering) planet, assuming the planets are ringless and have the same radii R_P . The planets differ only in their surface scattering properties. Albedos are shown for visible red light ($0.6\text{-}0.7\mu\text{m}$).

the three planets.

The full-disk albedo can be converted into the planet’s luminosity L_P as a fraction of star’s luminosity L_* for a planet of equatorial radius R_P at an orbital distance D_P .

$$L_P/L_* = (R_P/D_P)^2 \cdot p \quad (9)$$

For example, for Saturn at 1 AU, $(R_P/D_P)^2 \approx 1.6 \times 10^{-7}$. The abscissa of Fig. 6 indicates the azimuthal angle of the planet in its orbital plane, or the orbital angle Θ (see Fig. 1), starting at minimum planet phase ($\Theta = -180^\circ$). Note that only for edge-on inclinations does the minimum phase along the orbit correspond to a completely “new moon”. For orbits with lower inclinations, the minimum phase would be a crescent of a size between “new moon” and “half moon”. The corresponding maximum phase will be between the “full moon” and “half moon” at $\Theta = 0^\circ$. For circular orbits, the plot can be transformed into a time-dependent light curve simply by dividing Θ by 360° and multiplying by the planet’s orbital period.

Study of the spectral dependence of reflected light curves is beyond the scope of this paper; we will address this in a future paper. We do note, however, that Fig. 3 indicates that at shorter wavelengths Jupiter is less forward scattering than at longer wavelengths. Also, Figs. 3 and 4 indicate that both Jupiter and Saturn are darker in blue than in red at observational geometries close to back scattering ($\alpha \approx 0^\circ$).

The light curve for Jupiter peaks much more sharply at full phase ($\Theta \approx 0^\circ$) than the light curves of Saturn or the Lambertian planet because of the sharp back-scattering peak in Jupiter’s scattering phase function ($\alpha \approx 0^\circ$ in Fig. 2). Near zero phase ($\Theta \approx \pm 180^\circ$ in Fig. 6), Jupiter is more luminous than the other two models due to the large forward scattering from its surface ($\alpha \approx 180^\circ$ in Fig. 2).

Such differences in phase functions is commonly attributed to larger particle size for the main cloud deck on Jupiter. For example, Tomasko et al. (1978) suggest particle sizes larger than $0.6 \mu\text{m}$ to explain the forward scattering.

3.2. Oblate Planets

Saturn’s equatorial radius is 10% larger than its polar radius. This 10% oblateness of Saturn (6% for Jupiter) makes the planet appear larger when looking from the pole than when looking from the equator, which affects the light curves.

Figure 7 compares light curves for a spherical planet, a 10% oblate planet viewed from its equator, and a 10% oblate planet viewed from 45° latitude. All three sample planets have the same equatorial radius and scattering properties of Saturn. The light curves in Fig. 7 are displayed for an edge-on orbit ($i=90^\circ$) of a planet rotating “on its side” ($\epsilon=90^\circ$), because this geometry emphasizes the effects of oblateness in the reflected light. The differences among the curves is created by differences in the observer’s azimuth relative

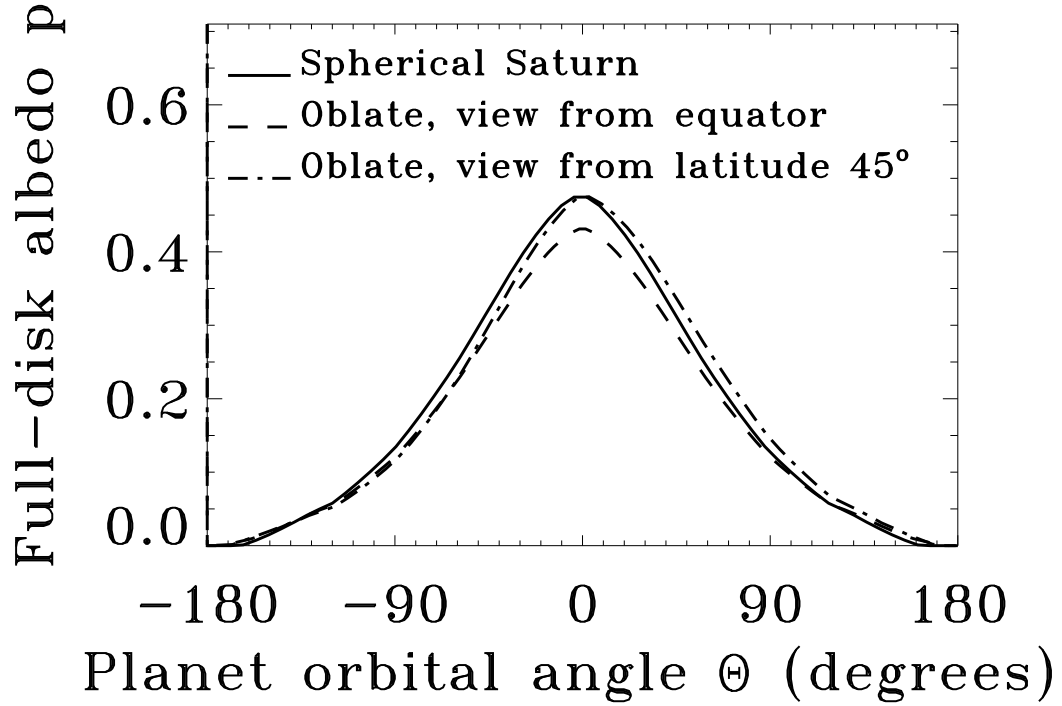


Fig. 7.— Comparison of light curves for a spherical and a 10% oblate planet with Saturn’s surface properties. Planets have the same equatorial radii and are ringless. The orbit is observed edge-on ($i=90^\circ$). The planets are rotating “on their side” ($\epsilon=90^\circ$). Albedos shown are for visible red light ($0.6\text{-}0.7\mu\text{m}$).

to the planet’s equator. (This angle is analogous to ω_r but is measured with respect to the equatorial plane rather than the ring plane. The rings are in the equatorial plane for Saturn and thus the same ω_r characterizes the observer’s azimuth.) Observing the planet from the equator decreases the cross-section of the planet and thus decreases the amplitude of the curve. Observing the planet from the pole yields a curve indistinguishable from the solid curve for a spherical planet; this is not shown in Fig. 7. Observing the planet from latitude 45° produces a small asymmetry in the curve because on one side of the orbit the flatter (and larger in projection) pole is better illuminated than on the other side of the orbit. This asymmetry is small compared to the asymmetries produced by rings, as we discuss in the next section.

3.3. Ring effects

The presence of rings has a large effect on the light curves of planets in reflected light. In order to describe the geometry of ringed planetary systems, two more parameters are required; even assuming a fixed radial density distribution for the rings, the geometry becomes sensitive to the ring obliquity ϵ (the angle between the ring and ecliptic planes), and to the azimuth of the observer relative to the rings ω_r (see Fig. 5). Together with the variable orbital inclination i , this produces the three-parameter space that we have sampled to explore possible light curves for ringed exoplanets similar to Saturn.

Figure 8 shows an example light curve for $i=55^\circ$, $\epsilon=27^\circ$ and $\omega_r=25^\circ$, which is a convenient geometry to demonstrate different ring effects in one light curve. The cartoon on the right of Fig. 8 displays images of Saturn at several positions on the orbit as it would appear to a remote observer. The plot on the left shows the light curve for the ringed planet (+ symbols) compared to the curve for the same geometry for a ringless planet (solid curve). The $\sim 10\%$ spread of the points in the ringed light curve is due partially to the large steps in the ring reflection table (see Fig. 2) and should be treated as a model uncertainty. For a large fraction of the orbit, the ring presence increases the luminosity of the planet ($\Theta < -20^\circ$) because the observer is able to view more reflecting surface. However for $0 < \Theta < 100^\circ$ the rings are not well illuminated and in fact shadow part of the planet, producing a lower luminosity than for the non-ringed planet. More importantly, the ringed light curve is asymmetric, which makes it distinguishable from any light curves of a non-ringed planet on a circular orbit. Obviously, planets on eccentric orbits may produce asymmetric curves due to variation in planet-star separation along the orbit. Light curves for non-ringed planets on eccentric orbits thus could be confused with those of ringed planets in the absence of radial velocity data (see Section 3.4 for discussion).

The variety of light curves for a Saturn-like planet at different geometries is illustrated in Figure 9. In this figure, different ring’s obliquities are shown in each subplot as black curves. The solid black curve indicates an obliquity of $\epsilon=89^\circ$ (that is, the planet is rotating

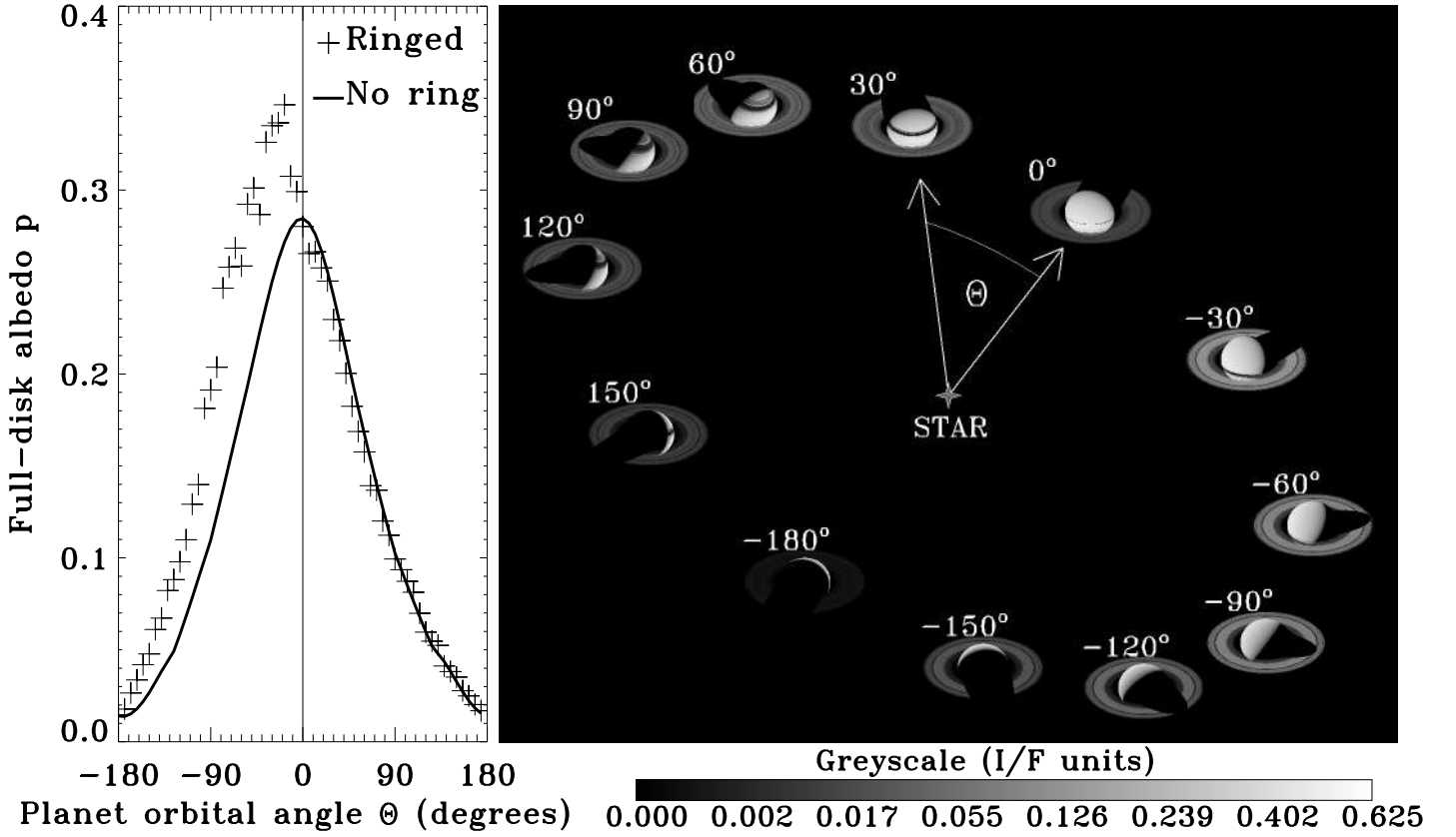


Fig. 8.— Effect of Saturn’s rings if observed at 35° above the orbital plane ($i=55^\circ$). In this example, Saturn’s ring’s obliquity is $\epsilon=27^\circ$. The observer’s azimuth on the ecliptic is separated from the intersection of the ring and ecliptic planes by $\omega_r=25^\circ$. The plot on the left shows light curves for a ringless planet (solid curve) and for a ringed planet (crosses). Values of Θ are indicated next to each image. The brightness of the images in the cartoon is given in the units of I/F , as indicated on the nonlinear greyscale bar.

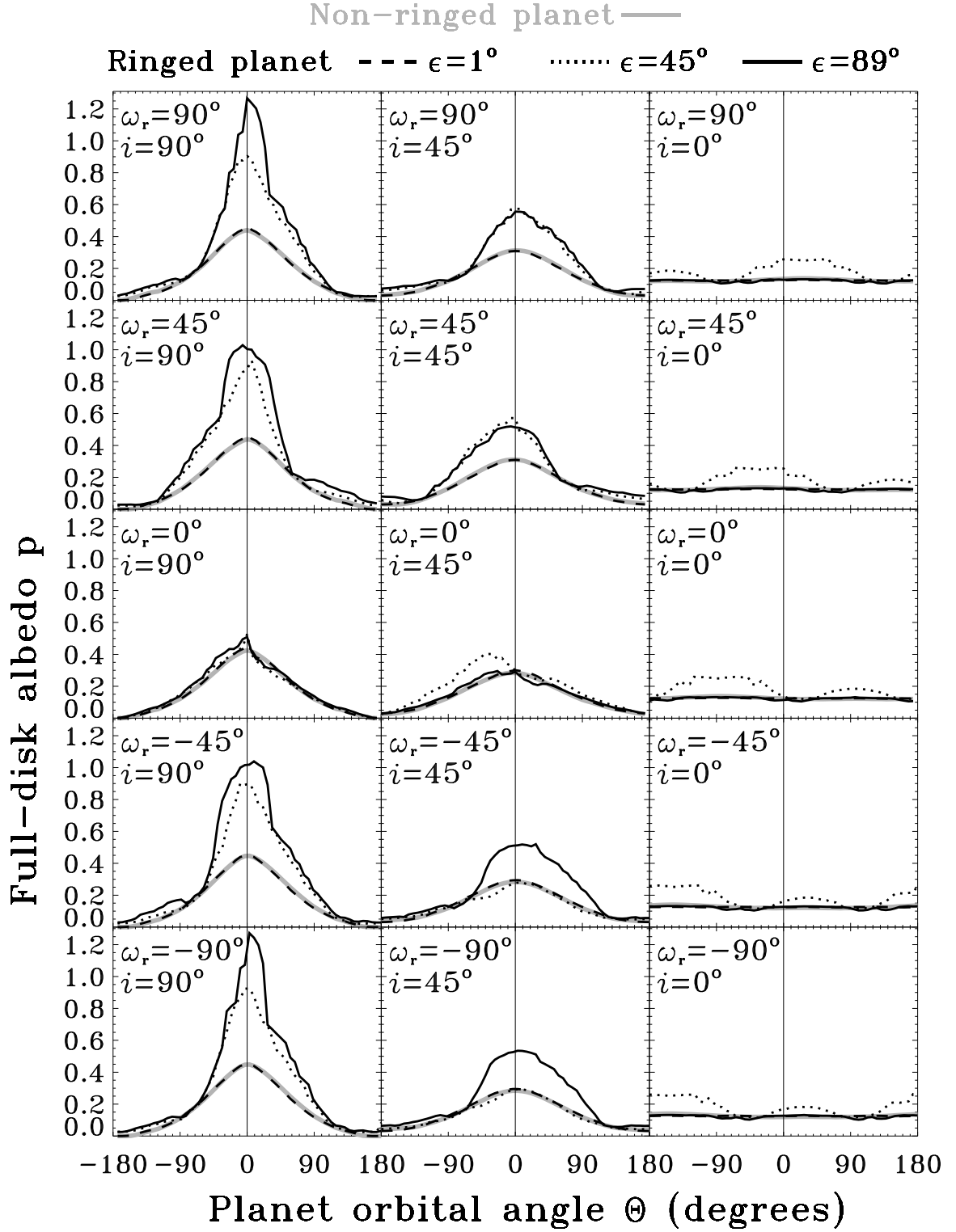


Fig. 9.— Light curves for Saturn for different geometries. Different ring obliquities ϵ are shown on each subplot as black curves. A curve for a spherical planet without rings is shown on each subplot in grey. Each column corresponds to a different orbital inclinations i . Each row corresponds to a different azimuth ω_r of the observer relative to the rings.

on its side, and rings are located in the equatorial plane and are nearly perpendicular to ecliptic). The dotted black curve is for $\epsilon=45^\circ$, and the dashed black curve is for $\epsilon=1^\circ$ (rings are nearly in the ecliptic plane). Grey curves illustrate the same geometries for a non-ringed planet.

Each subplot within Fig. 9 corresponds to a different observer geometry. In the left column, the orbit is observed edge-on ($i=90^\circ$); the middle column corresponds to an observer 45° above the ecliptic ($i=45^\circ$); the right column shows the orbit observed face-on ($i=0^\circ$). Each row corresponds to different azimuths of the observer relative to the rings ω_r . The top row illustrates geometries with $\omega_r=90^\circ$. At this azimuth, the rings are seen at the maximum possible opening, assuming all other geometric parameters (ring obliquity ϵ and orbital inclination i) are fixed. In lower rows, the observer’s azimuthal is rotated with respect to the orbital plane, resulting in a more grazing view of the rings. The bottom row is for $\omega_r=90^\circ$, for which the rings are seen at the most grazing geometry possible for fixed ϵ and i .

Several lessons can be learned from Fig. 9. First, rings generally increase the amplitude of the light curves by a factor of two to three. Recall that precise, but unresolved observations will only be able to detect the variations on top of the large constant flux of the star. An amplitude increase due to rings could be partially confused with effects of due to a larger planet size or albedo. The ambiguity may be resolved spectrally because the spectrum of rings should be rather flat, whereas the planetary atmosphere is expected to be dark at a set of prominent gaseous absorption bands.

The second lesson is that light curves for a ringed planet display two types of asymmetry. The first, and potentially easier to detect, asymmetry is the offset of the curve’s maximum relative to $\Theta = 0^\circ$, the maximum point for light curves of a ringless planet (marked by vertical lines in Fig. 9). This offset of the light curve maximum itself occurs in rather small fraction of the plots. However, since the entire curve is asymmetric, the effect would be detectable as an overall deviation from the simple symmetric curves likely to be used to fit the first detections of reflected light. If radial velocity data exist for such a planet, the exact timing of the $\Theta = 0^\circ$ point and the eccentricity of the orbit would be measurable. In this case, a shifted maximum in the light curve would yield direct evidence of the rings when compared to the asymmetry expected for any orbit eccentricity.

The offset of the light curve maximum due to rings is a strong photometric signature that was also noted in the ring simulation of Arnold & Schneider (2004) (as a ϕ -shift). We stress here, however, that other processes may be capable of producing such a ϕ -shift. Similar, although probably smaller, shifts may be induced by seasonal brightness variation on the planet. None of the giant planets in the Solar System have pronounced seasonal brightness variations, but extrasolar planets may display seasons, in which case the variations induced by them may cause an offset of the brightness maximum. Offsets could also be produced by a global asymmetry of the brightness distribution over the planet. An example in the Solar System is the striped appearance of Jupiter. Jupiter’s brightness varies with latitude by as

much as 50% in broadband visible light (Smith & Tomasko 1984). A reasonable scenario in which an extrasolar planet’s poles are brighter than its equator would cause the planet to appear globally brighter in winter and summer, and darker at mid-seasons, which could induce a ϕ –shift. Oblateness of a planet may also produce a small ϕ –shift (see Section 3.2). Again, spectroscopy may help to resolve the ambiguity between asymmetries caused by rings and by processes on the planet surface.

Asymmetry is also apparent in the shape of the light curve, but resolving such detail would require another order of magnitude in the instrument sensitivity. If this fine structure of the light curves could be measured, however, detection of rings would be possible without the assistance of radial velocity data. The main source of uncertainty in ring detection from an asymmetric light curve is the possibility that the asymmetry is created by an eccentric orbit of the planet. The fine structure of the light curve for the planet on eccentric orbit would be rather different than the structure for most of the curves for a ringed planet, as we discuss in Section 3.4.

The third lesson that we can draw from Fig. 9 is that in the case of face-on orbits (right column), both radial velocity observations and precise photometry would give no signal for a non-ringed planet. A ringed planet, however, typically produces a double brightness maximum, as the rings are illuminated first from the observer’s side and then from the back side during the orbit (dotted curve). At obliquity $\epsilon = 89^\circ$ (solid curve), the rings are not visible because the observer is nearly in the ring plane. The observer is also unable to see the rings at $\epsilon = 1^\circ$ (dashed curve) because the star always lies (nearly) in the ring plane. These extreme geometries are not typical for the random observations; more typical intermediate geometries ($\epsilon = 45^\circ$, dotted curve) result in a double peak, which cannot be confused with a light curve for a non-ringed planet on a circular orbit. Only for rare geometries producing equal height of the two peaks, and in the absence of a detailed measurement of the curve’s shape, could these two maximums be confused with a curve for a planet with half the orbital period. Generally, the maximums will differ in height, indicating that both maxima belong to a single orbit. Double maxima can be produced in eccentric orbits, but these exhibit light curves with differing fine structure (see Section 3.4). We note, however, that a double peak may be generated by seasonal variations or by an uneven brightness distribution at the planet’s surface. For example, a planet with bright poles rotating “on its side” (rotation axis parallel to ecliptic) whose orbit is observed face-on would exhibit two maxima in its light curve.

3.4. Effects due to eccentric orbits

One of the primary differences between extrasolar planets discovered to date and those in the Solar System is the large range of orbital eccentricity displayed by exoplanets. As an example of the effect eccentricity may have on the light curve of a planet in reflected light,

Figure 10 shows light curves for exoplanet HD 108147b, assuming the equatorial radius and atmospheric properties of Jupiter.

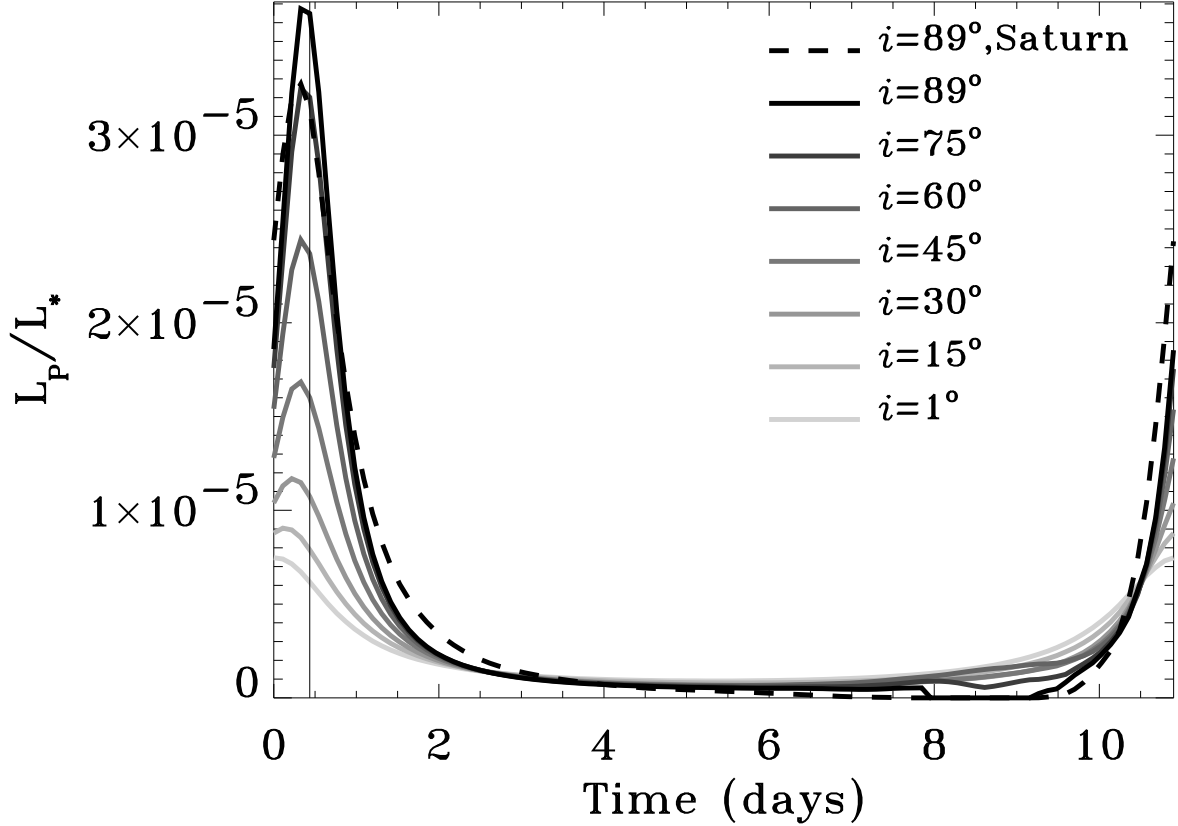


Fig. 10.— Light curves for the planet HD 108147b, assuming Jupiter’s equatorial radius and surface scattering properties, and 10% oblateness. The argument of pericentre is $\omega = -41^\circ$. The corresponding time of the maximum phase $\Theta = 0^\circ$, shown by the vertical line, is ~ 0.4 days after pericentre (which defines time zero). Different orbital inclinations from face-on to edge-on orientations ($i=1^\circ$ to $i=89^\circ$, respectively) are shown by lines of varying greyness. An edge-on light curve for a planet with Jupiter’s radius but Saturn’s surface properties is shown as a dashed line.

Prescribing Jupiter’s scattering properties to such a close-in planet is a questionable assumption. HD 108147b must be much hotter than Jupiter and may not have clouds at all or may have dark silicate or iron clouds (Sudarsky et al. 2003). Nevertheless, if clouds are present on this planet, the scattering of properties of Jupiter may roughly approximate the phase function and yield an order of magnitude estimate of the planet’s brightness (or, more

correctly, an upper limit to the brightness, since Jupiter’s clouds are nearly white).

In Fig. 10, we assume the planet to be 10% oblate, as is Saturn. The planet’s luminosity L_P is normalized by the star’s luminosity L_* , and is plotted versus time. We plot the light curve over one complete orbit, beginning at pericentre. The orbital parameters are those determined for HD 108147b by precise radial velocity measurements (Pepe et al. 2002). We have chosen to model HD 108147b because of its high eccentricity ($e = 0.498$) and relatively short semi-major axis ($a = 0.104\text{AU}$), which accentuates the effects of orbital eccentricity. Since the inclination of the orbital plane is not determinable from radial velocity measurements, we display light curves for different inclinations between $i=90^\circ$ (edge-on) and $i=0^\circ$ (face-on). The azimuthal location of the pericentre relative to the observer can be derived from the radial velocity measurements. For this HD 108147b, the argument of pericentre is $\omega = -41^\circ$, which means that we are fortunate to be at the azimuth at which the fullest planet phase $\Theta = 0^\circ$ is separated from pericentre by only 41° . With such a geometry, the phase-induced and eccentricity-induced maxima on the light curve amplify one another. As a result, the amplitude of the curve for the edge-on case is about 3.5×10^{-5} , nearly five times larger than in the face-on case, where only orbital distance variation matters. Because planets with edge-on orbital inclinations are detected more easily via radial velocity measurements, the chances of seeing an edge-on planet with a large light curve amplitude in follow-up observations is rather high.

The light curves of Fig. 10 can be rescaled easily for a planet with the same orbital eccentricity but different semi-major axis a_1 by multiplying the luminosity by $(a/a_1)^2$ and multiplying the time axis by the ratio of the orbital periods $(a_1/a)^{3/2}$.

In order to illustrate the importance of the argument of pericentre in determining the light curves of a given system measured by the observer, Figure 11 shows model light curves for planet HD 108147b with the same parameters in assumed for Fig. 10, except that the argument of pericentre is now set to $\omega = 60^\circ$, rather than the true $\omega = 319^\circ$. This example also serves to demonstrate the key features of the light curves for eccentric orbits.

Light curves for orbits observed nearly edge-on ($i \approx 90^\circ$) show a primary peak when the planet presents its full phase to the observer. The amplitude of the reflected light at this peak is approximately $L_P/L_* = 6.5 \times 10^{-6}$. The amplitude of this primary peak is reduced considerably at lower inclinations, since the planet no longer exhibits full phase at the maximum phase position. Additionally, the position of this peak moves towards the pericentre as the inclination is lowered.

The edge-on light curve also displays a secondary peak located close to pericentre. This peak is due to the increase in reflected light corresponding to the smaller planet-star separation at pericentre. At lower inclinations, this secondary peak becomes the higher of the two peaks as the planet-star separation function dominates over the phase function. In the extreme case of $i = 0^\circ$, the phase function no longer affects the light curve (the planet displays a constant half phase), and the light curve is purely a function of the planet-star

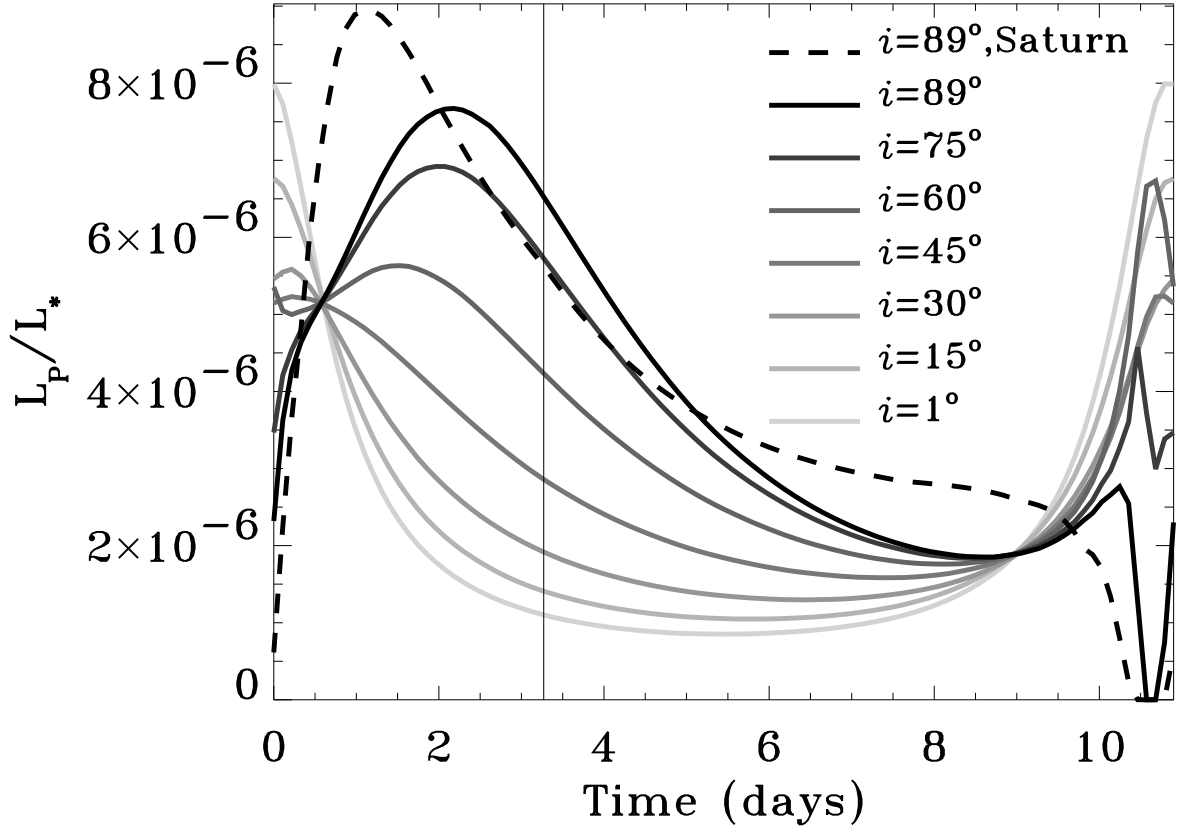


Fig. 11.— Light curves for a planet with the orbit of HD 108147b, but with an argument of pericentre $\omega = 60^\circ$. The planet has the radius and surface scattering properties of Jupiter. The time corresponding to maximum phase is shown by the vertical line, and is ~ 3.3 days after the pericentre. The orbital inclination changes from face-on to edge-on orientations ($i=1^\circ$ to $i=89^\circ$ respectively), as the line color changes from light grey to black. An edge-on light curve for same planet, but with Saturn’s surface scattering is shown as a dashed line.

separation.

The $i \approx 90^\circ$ and $i = 75^\circ$ light curves are complicated by the appearance of a sharp trough where the amplitude of reflected light is reduced almost to zero. This trough is due to the planet showing no phase (“new moon”) at this point of its orbit, and is particularly sharp due to the planet’s high angular speed at this point in its orbit. The trough is not prominent in lower inclinations because the minimum phase of the planet is no longer close to zero.

The double peaks are rather rare; for most values of ω they do not appear at any orbital inclination. If the planet’s surface is not as forward-scattering as is Jupiter’s (e.g., Saturn), the second peak is even less likely to appear. However, when the second peak is present, it is necessarily accompanied by the sharp trough immediately next to it. This feature makes the double-peaked light curve of an eccentric orbit distinguishable from the double-peaked light curve of a ringed planet, for which the two peaks are broad (see Section 3.3).

Single-peaked curves from eccentric orbits or ringed planets may be distinguished even without radial velocity data because the curve is smooth in the eccentric case. Although both ringed planets and eccentric orbits may result in an asymmetric light curve, the complicated shadowing of a ringed planet creates abrupt variations along the curve (see Fig. 9).

The location of the light curve maximum relative to the pericentre can yield important constraints on the geometry of the orbit and the cloud cover of the planet. First, the orbital inclination is restricted by the amount of the temporal shift in the light curve maximum from pericentre. As the inclination increases, the maximum moves from pericentre (time zero in Figs. 10 and 11) toward the time of the maximum phase $\Theta = 0^\circ$ (the vertical line in Figs. 10 and 11). This shift is larger when the orbit is viewed from a position that places pericentre close to half-phase ($\omega \sim 0^\circ$ or $\omega \sim 180^\circ$) rather than “new moon” ($\omega \sim 90^\circ$) or “full-moon” ($\omega \sim -90^\circ$) phases. Unlike the amplitude of the curve, which is also an indicator of inclination, the shift cannot be alternatively produced by altering the planet’s size or albedo. However the shift can result from a different strength of backscattering at the planet’s surface. An example of such ambiguity is the edge-on light curve for a planet with Saturn’s scattering properties (dashed line in Fig. 11), which has a maximum where a Jupiter’s curve of $i \approx 50^\circ$ would have its maximum. The ambiguity may be resolved by comparing the detailed shape of the curves.

Second, the curve’s maximum shift may also serve to restrict the surface properties of the planet. Although the shift can be confused with the effect of orbital inclination, a lower limit may be put on the strength of backward scattering for the planet’s surface. For each type of scattering surface, a maximum possible shift of the curve’s peak from pericentre towards $\Theta = 0^\circ$ occurs in the face-on case ($i = 0^\circ$). If a larger shift is observed, it can only be explained by a sharper backward scattering peak of the surface. Constraining surface properties in this way should be treated with caution, however, because of possible contamination by rings (we did not model both rings and eccentric orbits simultaneously),

large-scale bright patches on the planet’s surface, or seasonal variation of the cloud coverage.

Figure 12 illustrates the sensitivity of the shift to the inclination of the orbit (displayed along the ordinate of each subplot) and different atmospheric scattering (each of the three columns of subplots). The right side of each subplot ($\omega = -90^\circ$) corresponds to observations from the apocentre side of the orbit. At such a position, the planet is observed at its fullest possible phase ($\Theta = 0^\circ$) at pericentre, and since the eccentricity-induced and phase-induced maxima in the light curve coincide at pericentre, the shift between the light curve maximum and pericentre is zero. The left side of each subplot ($\omega = 90^\circ$) corresponds to observations from the pericentre side of the orbit. Here the planet is observed at its smallest possible phase ($\Theta = 180^\circ$) at pericentre, so that the eccentricity-induced maximum is shifted from the phase-induced maximum by half the orbital period. The maximum of the combined light curve then has a complicated dependence on e , i and planet’s scattering properties. In the simple case of $e = 0$, the eccentricity-induced maximum does not exist, and the curve’s maximum is always at the fullest phase. In this case, the time of the maximum follows the observer’s position ω , with the shift reaching half phase at $\omega = 90^\circ$ (red at the left on all $e = 0$ plots).

If radial velocity data exist for the planet, then the orbital eccentricity e and argument of pericentre ω are known, and the shift, indicated by the color coding in Fig. 12 is observable. The orbital inclination i (shown on the ordinate) is generally not known. Orbital inclination is known for transiting planets ($i \approx 90^\circ$), but is only very loosely constrained in the absence of a transit to $i < (90 - \Delta)^\circ$, where Δ is a small angle depending on the planet’s size and planetary system’s geometry.

Our method of constraining the orbital inclination i is achieved by matching a measured time shift value with those along the vertical line corresponding to the known ω on the plot with the appropriate eccentricity, as measured by radial velocity techniques. For example, a planet with Jupiter’s scattering properties on an eccentric $e=0.4$ orbit, observed to have a temporal shift of 20% of the orbital period (green) by an observer with $\omega \approx 45^\circ$, would imply inclinations of $60\text{--}90^\circ$. A shift of 10–15% of the orbital period (light blue) would mean orbital inclinations of $30\text{--}60^\circ$, while shifts smaller than 10% (purple to black), would mean inclinations of $0\text{--}30^\circ$. An ambiguity remains due to the unknown scattering properties of the planet’s surface. Three examples of the scattering are shown in the three columns of Fig. 12: a strongly backward scattering Jupiter, a weaker backward scattering Saturn, and the less realistic extreme case of Lambertian surface. Back scattering stronger than that exhibited by Jupiter may exist on extrasolar planets. We did not model this case, but expect that such an extreme example would produce a column of plots to the left of the Jupiter column, following the trends back scattering increases from Lambertian on the right to Jupiter on the left.

Examination of the columns for Jupiter, Saturn and Lambertian surfaces indicates that

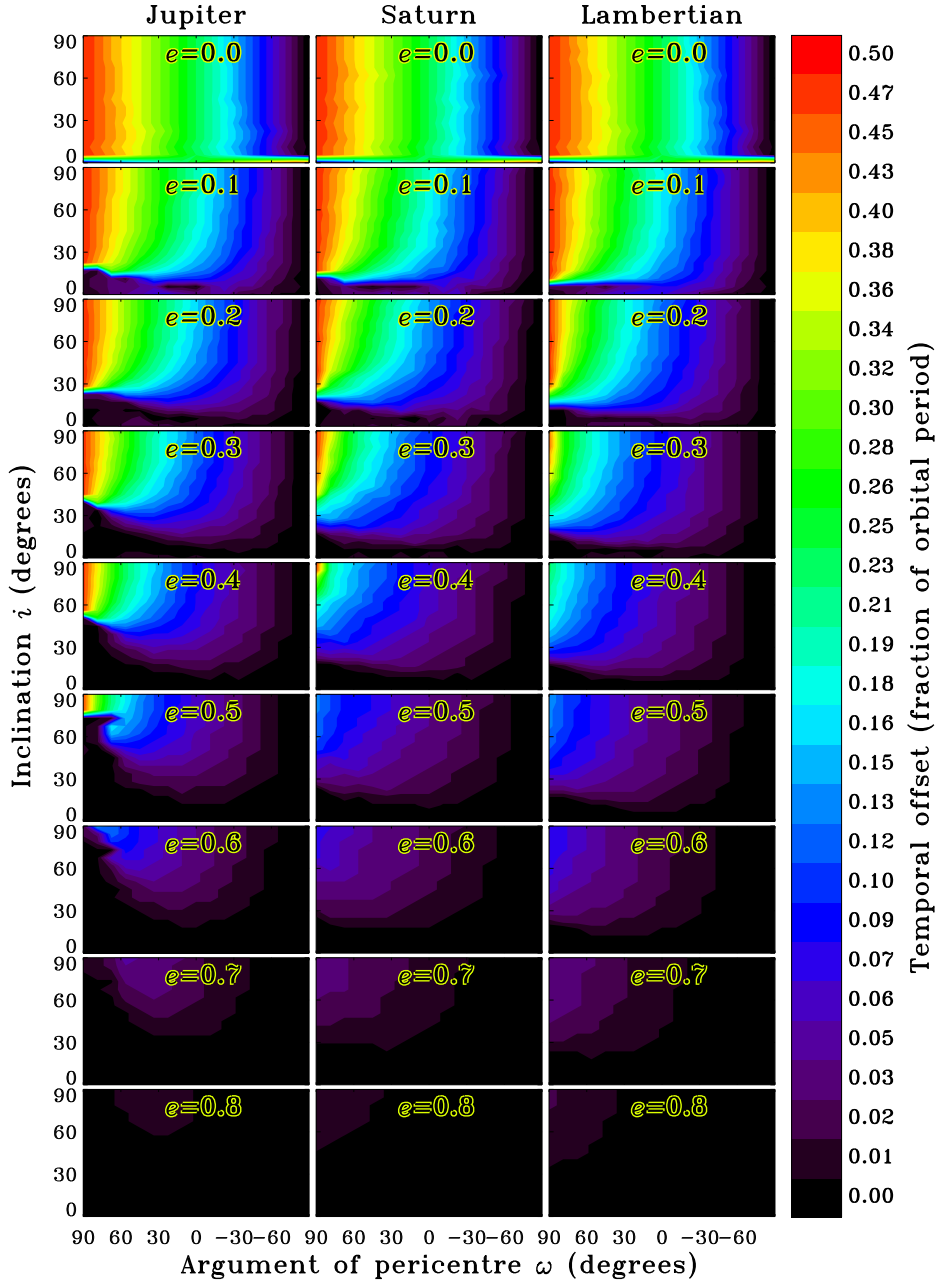


Fig. 12.— Summary of the temporal shift of the light curve maximum from the pericentre for eccentric orbits at different observational geometries for planets with Jupiter-like (left column), Saturn-like (middle column), and Lambertian scattering properties. Shifts are measured as a fraction of the orbital period. Each planet is assumed to be 10% oblate. The eccentricity of the orbit increases from the top row of subplots to the bottom row. Viewing geometry is described by the orbital inclination and argument of pericentre, plotted on the ordinate and abscissa, respectively of each subplot.

in some cases, scattering properties may be inferred from observation of the temporal shift in the reflected light. In some geometries a strong temporal shift may be observed at given e and ω . For example, if $e = 0.4$, $\omega=60^\circ$, and the observed shift is 25% the orbital period, only the left plot corresponding to Jupiter-like scattering displays green anywhere along the $\omega=60^\circ$ vertical line; thus only strongly back scattering planet like Jupiter can be consistent with the observation.

The contrast, or difference between the maximum and minimum amplitude of the light curve, gives a measure of the degree of variability that the planet’s reflected light displays. It is this variation that new generation space or ground-based photometers may be able to detect if they can achieve the required levels of precision. The largest contrast is observed for edge-on, $i = 90^\circ$, orbits (see Fig. 11), while at lower inclinations the contrast is reduced. However at very low inclinations approaching $i=0^\circ$, the contrast increases again as the amplitude of reflected light at the pericentre increases. Since the contrast at $i=0^\circ$ is higher than at mid inclinations, measuring reflected light may provide a method of detecting planets with face-on orbits, so long as the planet’s orbit is highly eccentric. Reflected light observations would then complement other methods, such as radial velocity measurements, that are unable to detect planets orbiting with face-on orientations.

We plot the light curve contrast for all possible orbital orientations in Figs. 13. Note that the backward scattering peak of Jupiter’s surface makes the planet much darker at low inclinations than Saturn or Lambertian planet. These contour maps display the degree of contrast for various orbital inclinations and arguments of pericentre at given eccentricities. At a given orientation, the more eccentric orbits show much higher contrast than circular orbits, although the amount of contrast is strongly dependent both on inclination and argument of pericentre. At high eccentricities, favorable geometries (such as $i = 90^\circ$ and $\omega = -90$) can increase the contrast by approximately five times that of less favorable orientations.

4. Discussion

4.1. Uncertainties

Our model provides a rather accurate description of reflected light curves for Jupiter and Saturn. The largest uncertainties are due to the lack of observations at large phase angles (forward scattering at $\alpha > 150^\circ$) for the surfaces of Jupiter, Saturn, and its rings. The extrapolations we have made to the phase functions could result in a factor of a few error in the brightness at these angles. Luckily, the luminosity of the planet at forward-scattering geometries is small because of the small area of the illuminated crescent at those positions. Consequently, this uncertainty does not influence the large amplitude features of our modeled light curves. The maxima of the highest-amplitude (edge-on) light curves,

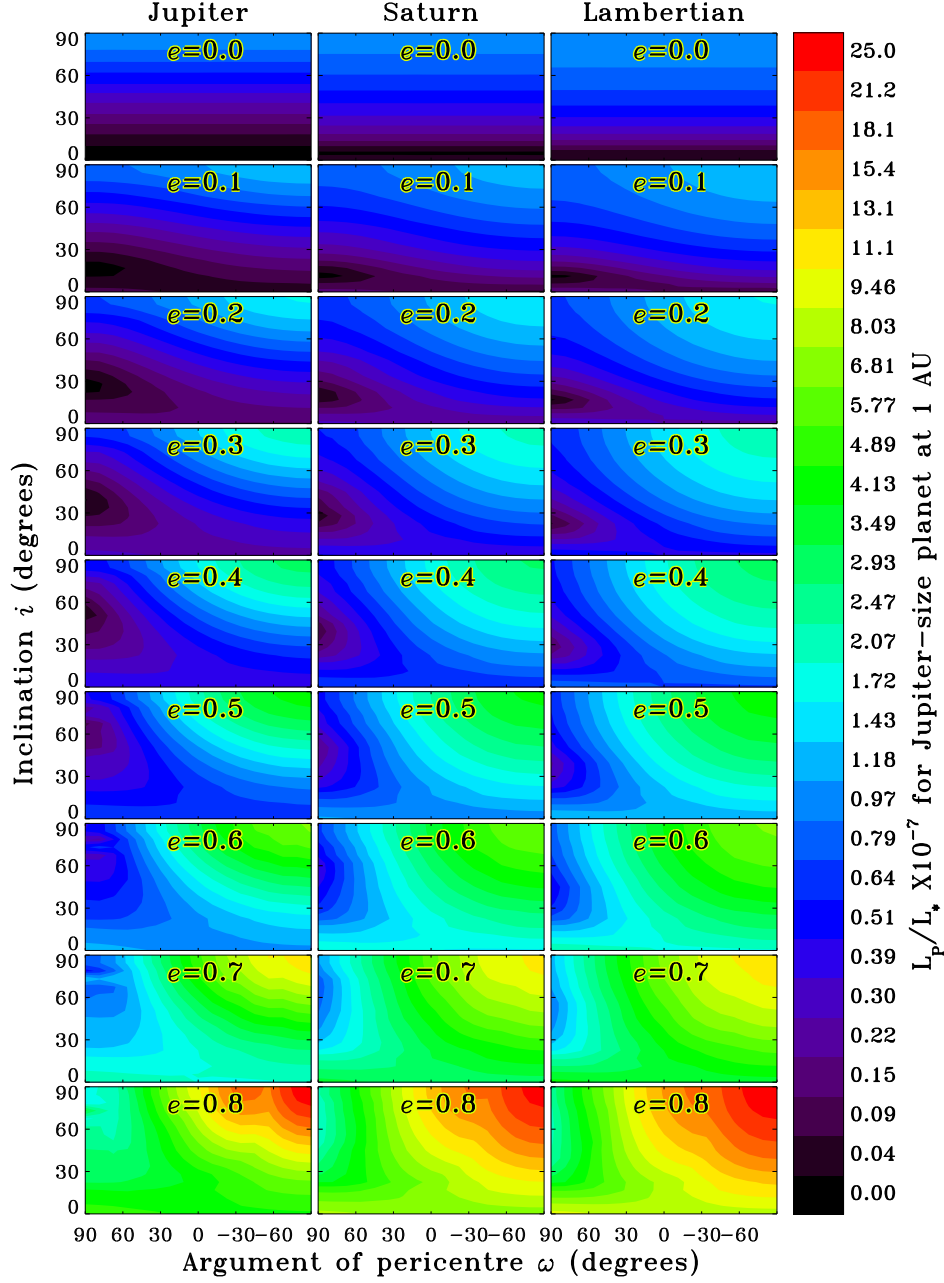


Fig. 13.— Summary of light curve variability amplitudes, or contrast, for eccentric orbits at different observational geometries for Jupiter (left column), Saturn (middle column), and Lambertian scattering properties with surface albedo 0.82 (right column). Planets are assumed to be 10% oblate.

which happen at opposition, can be constrained to within a few percent by high spectral resolution ground-based data for Saturn and Jupiter. In our study, the uncertainty of these maximum amplitudes is 10-20% because the brightness of a planet varies with wavelength by about the same amount within the 0.6-0.7 μm spectral range (Karkoschka 1998).

Reflectivity of the rings may be in error by as much as 50% because many geometries, especially those for face-on ring illumination and face-on ring observation, are not constrained by observations. Face-on illumination never happens for Saturn’s rings because of its 27° obliquity. Observations of the rings face-on are unavailable because all spacecraft visiting Saturn have had trajectories close to ecliptic. New observations by the Cassini spacecraft (arriving at Saturn in July 2004) will fill this gap in the data. Another source of the ring error is the coarse grid in the tabulated ring scattering properties (see Section 2). This grid-induced noise is usually below 30% of the ring’s luminosity.

Rings around close-in, short-period exoplanets may be unlikely because of tidal disruption, and in any case can only consist of rock. (Saturn’s rings are 99% ice.) Ice rings are stable against evaporation outside ~ 7 AU for solar-type stars (Mekler & Podolak 1994). Rocky ring material would probably be several times darker than ice, but would remain backward scattering for geometric reasons. Indeed, the rocks in Saturn’s rings behave as moonlets and are bright at backward-scattering full-phase geometry. Ring density for extrasolar planets is difficult to predict. It is possible that rocky rings of extrasolar planets are massive and optically thick. An example in the Solar System is Earth, which may have had massive rings while the Moon was forming. Furthermore, ring size for exoplanets may be very different from Saturn’s rings, which would have a large effect on the ring luminosity. We do not model various ring sizes here and refer the reader to the work of Arnold & Schneider (2004) which investigates ring size effects. The optical depth of any rings around extrasolar planets may also differ substantially from that of the rings of Saturn. It is important to note that when a ring has an optical depth more than about 3-5, the brightness of illuminated side becomes insensitive to further increases of optical depth. More than half of the area of Saturn’s rings has an intermediate optical depth of 0.5-3, which can be considered neither optically thin nor optically thick. These optical depths cause the dark side of Saturn’s ring to be quite bright. If the rings of an extrasolar planet are denser than Saturn’s, the ring-induced light curves will be more asymmetric due to the difference between the dark and bright sides of the rings. If the rings are optically thin, some asymmetry due to shadows will remain, but the light curve asymmetry due to the different sides of the ring will decrease. Since most of Saturn’s rings are quite dense, the brightness of the illuminated side is nearly equal to the “saturated” brightness achieved at infinite optical depth. For this reason, we do not expect that an increased optical depth in any extrasolar rings will result in a large increase over what we predict here in the brightness at the light curve maximum. The effects of differences in ring size or ring particle albedo are likely to be more prominent.

Application of our model light curves for the bodies of Jupiter and Saturn to the bodies of close-in giant exoplanets, whose bright light curves will be the most observable, has

a number of complications related to chemistry. The clouds on these exoplanets are expected to be composed of solid Fe, MgSiO_3 , Al_2O_3 , and other condensates that are stable at high temperatures (Seager et al. 2000; Burrows & Sharp 1999), rather than the water and ammonia ices seen in Solar System giants (Weidenschilling & Lewis 1973). These clouds may be darker and the corresponding light curve amplitudes may be several times smaller. For spherical particles, the scattering phase function depends on size of the particle compared to the wavelength of light, and on particle composition. Consequently, it is possible that forward and backward scattering maxima typical of Jupiter and Saturn could occur for cloud-covered exoplanets even if their cloud composition is different. Remarkably, the direct spectral signature of ammonia or water ice particles is found in small weather patches that cover only a few percents of Jupiter’s area (Simon-Miller et al. 2000; Baines et al. 2002). Most of the area is covered by clouds that exhibit no signature of ice on the surface of the particles. This may be due to the coating of the condensate particles by photochemically produced materials. Whether the photochemistry on extrasolar giant planets could alter the surface of cloud particles is beyond the scope of this paper, but direct comparison of clouds made of pure silicate on extrasolar planets, for example, with clouds made of pure ammonia on Jupiter and Saturn is probably oversimplified. The most important parameter in determining the brightness of a planet is the presence or absence of clouds, which depends on poorly-known (even for Jupiter and Saturn) vertical atmospheric circulation. Detection or non-detection of a light curve with the expected amplitudes would be most indicative of such cloud presence.

4.2. Prospects for Detection by Modern Instruments

Short-period giant planets are the easiest targets for detection by precise (spatially unresolved) photometry because they are well-illuminated by the star. As discussed in the last section, light curves for such planets may differ from the those we present here for Jupiter and Saturn because their hotter temperatures (and possibly different evolution as a result of migration) will alter the planet’s atmosphere and clouds and thus its scattering properties.

Nevertheless, our model light curves do provide a first-order approximation for a cloud-covered exoplanet and so we will discuss the model light curves of Jupiter and Saturn as if they were extrasolar planets placed at small orbital distances. In that case, our light curve amplitudes (Figs. 6 to 9) can be converted to measurable units of fractional luminosity L_P/L_* using Eq. 9. The ratio L_P/L_* depends inversely on the square of the planet’s orbital distance, and is independent of the star’s distance to the observer. Typical extrasolar planets discovered to date have orbital distances (semi-major axes) between 0.3 and 3 AU, corresponding to conversion factors of 2.5×10^{-4} to 2.5×10^{-8} multiplying the order-of-unity light curve amplitudes displayed in Figs. 6 to 9, assuming that the planet has a radius equal to that of Jupiter’s at 71400 km. For convenience, we have scaled amplitudes in Fig. 13 to a planet with a semi-major axis equal to 1 AU.

The ability of precise space-based photometers such as MOST and KEPLER to detect reflected light from extrasolar planets depends on the signal-to-noise (S/N) of the observations, and thus the apparent brightness of the target parent star. Precisions approaching 10^{-6} are expected for stars as bright as 6th magnitude or brighter in V band ($V \leq 6$) with MOST (Green et al. 2003; Walker et al. 2003), and $\sim 67 \times 10^{-6}$ for stars as faint as $R = 12$ in R -band⁵ with KEPLER (Jenkins & Doyle 2003; Koch et al. 2000; Jenkins et al. 2000; Remund et al. 2001) independent of magnitude. Within a fiducial survey volume of radius 30pc, where a solar-type star would have $V \leq 7.2$ and $R \leq 6.9$, MOST and KEPLER would thus be able to provide measurements with precisions of $\sim 2 \times 10^{-6}$ and $\sim 6 \times 10^{-6}$, respectively, except where they are dominated by instrumental or stellar noise, which may decrease the sensitivity by factors of five for the faintest objects. For short-period planets, the S/N may be increased by repeated observations over several orbits. On the other hand, planets with periods longer than the order of several days may suffer more from confusion with fluctuations in stellar luminosity on the order of 10^{-5} (Jenkins & Doyle 2003). In summary, space-based photometers currently launched such as MOST (with no survey capability) and about to be launched (KEPLER, a survey instrument), should be able to detect variations in the total light received from stars within 30pc due to reflected light from orbiting planets at the level of 10^{-5} .

Direct, spatially-resolved imaging, of the sort that may be provided by future space instruments or adaptive optics on Extremely Large Telescopes (ELT) from the ground (both aided with coronagraphic or nulling techniques) may detect faint planets if they are sufficiently distant from the star to be separable from the angular size of the optical point spread function (Dekany et al. 2004; Lardi re et al. 2003; Codona & Angel 2004; Trauger et al. 2003; Krist et al. 2003; Clampin et al. 2001).

For example, Lardi re et al. (2003) used detailed simulations of ideal adaptive optics systems with different actuator pitches placed on ground-based ELT of various aperture sizes located in varying atmospheric conditions, to calculate the planet-to-star flux ratio that would be required in order to reach a signal-to-noise of three ($S/N = 3$) in one night’s observation (10 hour exposure). The planet-star flux ratio is related to, but could be slightly larger than the contrast values of Fig. 13, which show only the *varying* portion of the planet’s brightness compared to the (assumed) constant stellar brightness. Generally speaking, they conclude that a 30m-diameter ELT on one of the best sites in the world (e.g. Mauna Kea or in the Antarctic) could easily detect with $S/N = 3$ planets with brightness ratios as small as 1×10^{-9} over the range of projected planet-host star separations corresponding to 0.1 – 1.0 arcsec. These separations correspond to planets on orbits with semi-major axes from 1 to 10 AU for systems 10pc distant from Earth (and about a factor of ten greater at 30pc). Such planets are more likely to have the temperatures of Saturn and Jupiter, and thus the scattering properties we have assumed here. We note that a ratios of 1×10^{-9} is about 100

⁵We model wavelengths here that are more similar to the R passband than the V band.

times the bright, dark blue contrast levels shown in Fig. 13, indicating that most systems we have considered would indeed be detectable even if they orbited 10 AU from their host.

Projected onto the sky plane, a planet is most separated from its host star near half-phase, i.e., at $\Theta \sim \pm 90^\circ$ (Figs. 6 to 9). At these points the planet is not at its maximum brightness, but may still be detectable. Note too that Lambertian planets may underestimate amplitudes at half-phase of planets that scatter anisotropically (see Fig. 6). On the other hand, rings may increase the luminosity by a factor of 2 – 3 or more if the rings are larger than those of Saturn, increasing the chance of light curve detection, as would larger planets. Many technical challenges will have to be overcome before contrast levels of 1×10^{-9} become detectable. In this light, it is interesting to note that because planet size is not believed to grow substantially with planet mass above one Jupiter mass (Guillot et al. 1996), searching for the photometric signature of large rings of extrasolar planets (if they exist) may be an easier task than searching for the planets themselves.

5. Conclusions

We have examined the effects of rings, realistic scattering properties (i.e. those actually measured for Saturn and Jupiter), viewing geometry, and orbit eccentricity on the characteristics of reflected light from extrasolar planets, and their combined planet-host star light curve. In particular, we have noted signatures of ringed planets, and have indicated cases in which planetary rings may be distinguished from, or confused with, other effects.

In the following table, we summarize signatures of planetary rings on the light curves of their extrasolar planets, and note differences between ring effects and those of a non-ringed planet on an eccentric orbit, or planetary surface effects.

Signature	Rings	Eccentric orbit	Alternative
Light curve amplitude	increases by factors 2 – 3 ^a	increase depends on e	larger albedo or planet size
Double peak	rare smooth peaks	rare, sharp trough near one peak	surface asymmetry ^b or seasons
Large-scale asymmetry	common	common	surface asymmetry ^b , oblateness, or seasons
Fine light curve structure	abrupt changes	smooth	
Shift of curve max from $\Theta=0^\circ$ (with radial velocity data)	often	never for circular orbit, calculable for eccentric orbits	surface asymmetry ^b , oblateness, seasons, or back scattering ^c

^aFor Saturn-sized (relative to the planetary radius) rings.

^bPlanet-scale asymmetry of the brightness distribution, e.g., bright poles.

^cThe strength of the back-scattering peak of the planetary phase function changes the shift of the curve maximum relative to $\Theta = 0^\circ$, which is known within the range defined by the possible phase functions (see Fig. 12).

Our studies of planets with Jupiter-like, Saturn-like and Lambertian scattering properties on eccentric orbits hold the following messages for potential observers:

1. An anisotropically scattering planet is much fainter at half-phase ($\Theta=\pm 90^\circ$) than is a Lambertian planet.
2. Anisotropically-scattering planets are also much fainter at low inclinations than are Lambertian planets.
3. For many geometries, eccentricity of the orbit may increase light curve amplitude by a large amount compared to a planet on a circular orbit with the same semi-major axis (see Fig. 13)

4. The timing of the lightcurve maximum with respect to pericentre may be used to restrict the orbital inclination and atmospheric back scattering properties for a large fraction of possible geometries (see Fig. 12)

In summary, rings, eccentric orbits, and atmospheric scattering properties of exoplanets may be detected with future telescopes in the next decade or so by the effect they have on the light curve of the planet’s reflected light, and these effects may often be distinguished from one another by the shape of the observed light curve alone or with the aid of additional radial velocity data.

Acknowledgements

We thank R.A. West for useful references on Jupiter’s scattering. The work begun at NASA GISS while U.D. was supported by Anthony D. Del Genio under the Cassini Project.

REFERENCES

- Arnold, L. & Schneider, J. 2004, A&A, accepted
- Baines, K. H., Carlson, R. W., & Kamp, L. W. 2002, *Icarus*, 159, 74
- Barnes, J. W. & Fortney, J. J. 2003, *Bull.–Am. Astron. Soc.*, 923
- Benedict, G. F., McArthur, B. E., Forveille, T., Delfosse, X., Nelan, E., Butler, R. P., Spiesman, W., Marcy, G., Goldman, B., Perrier, C., Jefferys, W. H., & Mayor, M. 2002, *ApJ*, 581, L115
- Bouchy, F., Pont, F., Santos, N., Melo, C., Mayor, M., Queloz, D., & Udry, S. 2004, A&A, submitted
- Burrows, A. & Sharp, C. M. 1999, *ApJ*, 512, 843
- Charbonneau, D., Brown, T. M., Latham, D. W., & Mayor, M. 2000, *ApJ*, 259, 45
- Charbonneau, D., Noyes, R., Korzennik, S., Nisenson, P., Jha, S., Vogt, S., & Kibrick, R. I. 1999, *ApJ*, 522, 145
- Clampin, M., Ford, H. C., Illingworth, G., Petro, L., & JPF Science Team. 2001, *Bulletin of the American Astronomical Society*, 33, 1356
- Codona, J. L. & Angel, R. 2004, *ApJ*, 604, L117
- Collier Cameron, A., Horne, K., Penny, A., & Leigh, C. 2002, *MNRAS*, 330, 187

- Dekany, R., Stapelfeldt, K., Traub, W., Macintosh, B., Woolf, N., Colavita, M., Trauger, J., & Ftacclas, C. 2004, RASP, submitted
- Dones, L., Cuzzi, J., & Showalter, M. 1993, *Icarus*, 105, 184
- Green, D., Matthews, J., Seager, S., & Kuchnig, R. 2003, *ApJ*, 590
- Guillot, T., Burrows, A., Hubbard, W. B., Lunine, J. I., & Saumon, D. 1996, *ApJ*, 459, L35+
- Hatzes, A. P. 2003, in *ASP Conference Series*, Vol. 294, *Scientific Frontiers in Research on Extrasolar Planets*, ed. D. Deming & S. Seager (San Francisco: ASP), 523–528
- Henry, G. W., Marcy, G. W., Butler, R. P., & Vogt, S. S. 2000, *ApJ*, 529, L41
- Jenkins, J., Witteborn, F., Koch, D., Dunham, E., Borucki, W., Updike, T. F., Skinner, M., & Jordan, S. 2000, in (*SPIE*), 520
- Jenkins, J. M. & Doyle, L. R. 2003, *ApJ*, 595, 429
- Karkoschka, E. 1994, *Icarus*, 111, 174
- Karkoschka, E. 1998, *Icarus*, 133, 134
- Koch, D., Borucki, W., Dunham, E., Jenkins, J., Webster, L., & Witteborn, F. 2000, in (*SPIE*), 508
- Konacki, M., Torres, G., Jha, S., & Sasselov, D. 2003, *Nature*, 421, 507
- Konacki, M., Torres, G., Sasselov, D., Pietrzynski, G., Udalski, A., Jha, S., Ruiz, M., Gieren, W., & Minniti, D. 2004, *ApJ Letters*, 609, 37
- Krist, J. E., Clampin, M., Petro, L., Woodruff, R. A., Ford, H. C., Illingworth, G. D., & Ftacclas, C. 2003, in *High-Contrast Imaging for Exo-Planet Detection*. Edited by Alfred B. Schultz. *Proceedings of the SPIE*, Volume 4860, pp. 288-294 (2003)., 288–294
- Lardi re, O., Salinari, P., Jolissaint, L., Carbillet, M., Riccardi, A., & Esposito, S. 2003, in *Second Backaskog Conference on ELTs (SPIE and ESO)*
- Leigh, C., Cameron, A. C., & Guillot, T. 2003c, *MNRAS*, 346, 890
- Leigh, C., Cameron, A. C., Horne, K., Penny, A., & James, D. 2003b, *MNRAS*, 334, 1271
- Leigh, C., Collier Cameron, A., Udry, S., Donati, J., Horne, K., James, D., & Penny, A. 2003a, *MNRAS*, 346, L16
- Mekler, Y. & Podolak, M. 1994, *Planet. Space Sci.*, 42, 865

- Murray, C. D. & Dermott, S. F. 2001, *Solar System Dynamics* (Cambridge University Press)
- Pepe, F., Mayor, M., Galland, F., Naef, D., Queloz, D., Santos, N., Udry, S., & Burnet, M. 2002, *A & A*, 388, 632
- Remund, Q., Jordan, S., Updike, T., Jenkins, J., & Borucki, W. 2001, in (SPIE), 182
- Seager, S., Whitney, B., & Sasselov, D. 2000, *ApJ*, 540, 504
- Simon-Miller, A. A., Conrath, B. J., Gierasch, P. J., & Beebe, R. F. 2000, *Icarus*, 145, 454
- Smith, P. H. & Tomasko, M. G. 1984, *Icarus*, 58, 35
- Sudarsky, D., Burrows, A., & Hubeny, I. 2003, *ApJ*, 588, 1121
- Tomasko, M. G. & Doose, L. R. 1984, *Icarus*, 58, 1
- Tomasko, M. G., West, R. A., & Castillo, N. D. 1978, *Icarus*, 33, 558
- Trauger, J., Hull, A., Backman, D., Brown, R. A., Burrows, A., Burrows, C., Ealey, M., Ftaclas, C., Heap, S., Kasdin, J., Kuchner, M., Lindensmith, C., Lunine, J., Marcy, G., Sahai, R., Spergel, D., Stapelfeldt, K., Traub, W., & Woodgate, B. 2003, *American Astronomical Society Meeting*, 203,
- Udalski, A., Paczynski, B., Zebrun, K., Szymanski, M., Kubiak, M., Soszynski, I., Szewczyk, O., Wyrzykowski, L., & Pietrzynski, G. 2002a, *Acta Astronomica*, 52, 1
- Udalski, A., Pietrzynski, G., Szymanski, M., Kubiak, M., Zebrun, K., Soszynski, I., Szewczyk, O., & Wyrzykowski, L. 2003, *Acta Astronomica*, 53, 133
- Udalski, A., Zebrun, K., Szymanski, M., Kubiak, M., Soszynski, I., Szewczyk, O., Wyrzykowski, L., & Pietrzynski, G. 2002b, *Acta Astronomica*, 52, 115
- Walker, G., Matthews, J., Kuschnig, R., Johnson, R., Rucinski, S., Pazder, J., Burley, G., Walker, A., Skaret, K., Zee, R., Grocott, S., Carroll, K., Sinclair, P., Sturgeon, D., & Harron, J. 2003, *PASP*, 115, 1023
- Weidenschilling, S. J. & Lewis, J. S. 1973, *Icarus*, 20, 465